IEEE Access
Multidisciplinary | Rapid Review | Open Access Journal

Received October 16, 2019, accepted October 30, 2019, date of publication November 7, 2019, date of current version November 20, 2019.

Digital Object Identifier 10.1109/ACCESS.2019.2952112

Custom-Designed Electrically Small Huygens Dipole Antennas Achieve Efficient, Directive Emissions Into Air When Mounted on a High Permittivity Block

RICHARD W. ZIOLKOWSKI, (Fellow, IEEE)
Global Big Data Technologies Centre, University of Technology Sydney, Ultimo, NSW 2007, Australia
e-mail: richard.ziolkowski@uts.edu.au

This work was supported by the Australian Research Council under Grant DP160102219.

ABSTRACT System-on-Chip (SoC) applications include embedded systems and mobile computing platforms. They will play major roles in fifth generation (5G) wireless systems, notably with the many associated IoT (internet-of-things) devices. Their wireless functions are enabled, for example, by on-chip antennas (OCAs), i.e., the system elements that connect them to devices in their external environments. These antennas generally reside on a high permittivity dielectric, such as silicon, which unfortunately causes most of their emitted power to be directed into the dielectric rather than into free space. This feature is quite detrimental, i.e., it leads to a severe degradation of an OCA's radiation efficiency as a transmitter of information to an external receiver and similarly to its poor performance as a receiver since little of its pattern resides in free space, severely limiting its ability to capture power from an external transmitter. Similar issues exist for sensors and communication devices residing on a human body. While many integrated antenna styles have been developed in attempts to deal with these issues, their complexities and remaining inefficiencies remain a bottleneck to their widespread adoption. It is demonstrated analytically and numerically that Huygens radiating systems provide a unique solution to these high permittivity substrate problems. Custom-designed electrically small Huygens dipole antennas that lie on the interface between air and a high permittivity block are reported that efficiently emit the majority of their radiated power into the air region rather than into the dielectric.

INDEX TERMS Directivity, electrically small antennas, Huygens dipole antennas, on-body antennas, on-chip antennas.

I. INTRODUCTION

Antennas are key and essential components of any wireless system. At higher frequencies, the physical size of an antenna is small, e.g., a half-wavelength dipole at 100 GHz is only three millimeters long. This feature makes an antenna's integration with other electronic components directly on substrates such as silicon attractive and feasible. Thus, systems with integrated antennas are expected to be a common element that enables many internet-of-things (IoT) applications in the fifth generation (5G) ecosystem.

There are three major current schemes for the realization of an antenna with a front-end integrated circuit (IC). The first category is the antenna-in-package (AiP) technique, in which the antenna is implemented in the IC's packaging technology. In the second category the antenna is directly implemented on a silicon substrate and is popularly known as an on-chip-antenna (OCA). Finally, the third approach could be considered as a hybrid of an OCA and an AIP, i.e., the feed-point of the antenna is implemented on-chip while the radiating element itself is realized off-chip. Any of these designs must meet various practical requirements including, in particular, high radiation efficiencies.

OCAs alleviate the need for bond-wires that are needed to connect the antenna(s) implemented off-chip with the IC. The bond-wires themselves are generally not well characterized, especially at high frequencies where there is more loss due to impedance mismatches. Moreover, they also eliminate the

The associate editor coordinating the review of this manuscript and approving it for publication was Muhammad Zulfiker Alam.

requirement of sophisticated packaging technologies which are typically employed in AiP solutions. This strategy radically reduces the system's manufacturing costs. At the same time OCAs enable the realizations of highly compact systems, yielding significant area savings.

Fabrication technologies like CMOS facilitate the integration of an OCA with an IC for wireless devices for mobile computing, embedded systems, wireless power transfer, energy harvesting and other 5G and IoT (internet-of-things) applications. From a design point of view, all semiconductor technologies are roughly the same. They facilitate a multi-layer stack of dielectrics and metals. However, this also means the OCA will reside on a high permittivity substrate, such as silicon with a rather high relative permittivity of 11.7. Unfortunately, as will be reviewed and explicitly demonstrated, this configuration also causes most of the power radiated by an OCA to be directed into and confined in the substrate rather than being radiated into free space. This field behavior accounts for the significant degradation of the overall radiation efficiency of standard OCAs. Numerous approaches to overcome this critical feature have been reported including coated silicon lenses, ground shields, and matched dielectric interfaces [1]–[7]. Even metamaterial-inspired artificial magnetic conductors (AMCs) in the multilayered stack delineating the OCA have been considered [8]–[11]. Nevertheless, inefficient and complex OCAs still remain a bottleneck in the realization of various system-on-chip (SoC) applications. A truly efficient, simple OCA that overcomes these issues is highly desired.

Similar challenges are faced with on-body and wearable antennas [12], [13]. The relative permittivity of components of the body such as skin and muscle tissues is in the range of 40-50 [14]. Consequently, 5G IoT sensors and communication devices residing on a human body also face complicated antenna design and radiation efficiency issues.

It will be demonstrated analytically and numerically that custom-designed Huygens dipole antennas (HDAs) provide an elegant physical solution to achieve efficient antennas residing on high permittivity materials that radiate directive fields into free space. An HDA consists of a balanced pair of orthogonal electric and magnetic radiators which produces a broadside cardioid directivity pattern. A variety of HDAs have been successfully realized recently, e.g., [15]–[17]. They are based on tailored combinations of the metamaterial-inspired electric (Egyptian axe dipole, EAD) and magnetic (capacitively loaded loop, CLL) near field resonant parasitic (NFRP) elements driven by a printed electric dipole antenna. Custom-designed versions of these prototyped systems are developed herein for their placement on a surface of a finite-sized high permittivity dielectric block. The fundamental characterization of the Huygens-based approach to achieve efficient and directive emissions away from the block rather than into it will be first explored with one-dimensional (1D) analytical results (1D plane wave solutions to three dimensional canonical problems defined by two semi-infinite regions and infinite current sheets on the interface between them) and then three-dimensional (3D) numerical characterizations of electrically small, ideal two element (electric and magnetic) dipole arrays on the high permittivity block. Electrically small NFRP HDA designs matched to 50-Ω sources are then developed to conclusively demonstrate that nearly complete impedance matched, high directivity and highly efficient HDA-based antennas on finite-sized high permittivity substrates can be attained.

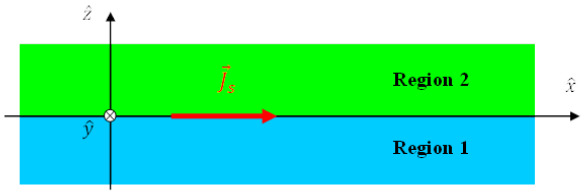

FIGURE 1. 1D analytical problem: Infinite electric current sheet on the interface between two 3D semi-infinite regions.

All of the simulated results reported herein were obtained with the ANSYS Electromagnetics Suite v17.0 using realistic material properties. Appendices provide additional details and cases of the 1D plane wave analyses and the 3D ideal radiators in relation to those discussed in the main text.

II. ANALYTICAL PROBLEMS AND HUYGENS SOURCE SOLUTION

A set of 3D canonical interface problems is treated first analytically in 1D to demonstrate the high permittivity dielectric problem and the HDA solution approach. An electric current sheet on the interface between a dielectric half-space and an air half-space illustrates the issues. A balanced combination of electric and magnetic current sheets on that interface then demonstrates the Huygens source solution. Additional details of these 3D electric and magnetic problems and their 1D analytical solutions are provided in Appendix A.

A. ELECTRIC CURRENT SHEET ON AN AIR-DIELECTRIC INTERFACE

The electric problem configuration is shown in Fig. 1. An electric current sheet

$$\vec{J}_s = J_0\,\delta(z)\,\hat{x} \tag{1}$$

is centered on the interface between two semi-infinite regions characterized by their permittivity and permeability values: Region 1, $z < 0$, ε_1 and μ_1 and Region 2, $z > 0$, ε_2 and μ_2. The corresponding impedance and wave numbers are $\eta_\ell = \sqrt{\mu_\ell/\varepsilon_\ell}$ and $k = \omega\sqrt{\varepsilon_\ell}\sqrt{\mu_\ell}$ for $\ell = 1, 2$. As detailed in Appendix A, the electromagnetic fields in each region (assuming an $\exp(j\,\omega\,t)$ time convention) are:

$$\begin{aligned}
\vec{E}_{\omega 2,e} &= -\frac{\eta_1\,\eta_2}{\eta_1+\eta_2}\,J_0\,e^{-j\,k_2\,z}\,\hat{x} \\
\vec{H}_{\omega 2,e} &= -\frac{\eta_1}{\eta_1+\eta_2}\,J_0\,e^{-j\,k_2\,z}\,\hat{y} \qquad (2)\\
\vec{E}_{\omega 1,e} &= -\frac{\eta_1\,\eta_2}{\eta_1+\eta_2}\,J_0\,e^{+j\,k_1\,z}\,\hat{x} \\
\vec{H}_{\omega 1,e} &= +\frac{\eta_2}{\eta_1+\eta_2}\,J_0\,e^{+j\,k_1\,z}\,\hat{y} \qquad (3)
\end{aligned}$$

where the "e" labels the electric current results. Consequently, the time-averaged power density in each region, i.e., the time-averaged Poynting vector $\left\langle \vec{S}_{\omega} \right\rangle = (1/2)\ \mathrm{Re}\left[\vec{E}_{\omega} \times \vec{H}^{*}_{\omega} \right]$, where * denotes the complex conjugate and the "bra-ket" notation denotes the time average, is

$$\begin{aligned} \left\langle \vec{S}_{\omega 2,e} \right\rangle &= = +\frac{1}{2} \frac{\eta_2 \, |\eta_1|^2}{|\eta_1 + \eta_2|^2} \, |J_0|^2 \, \hat{z} \\ \left\langle \vec{S}_{\omega 1,e} \right\rangle &= = -\frac{1}{2} \frac{\eta_1 \, |\eta_2|^2}{|\eta_1 + \eta_2|^2} \, |J_0|^2 \, \hat{z} \end{aligned} \tag{4}$$

Therefore, the ratio of the amount of power directed into each region is:

$$\frac{\left\langle \vec{S}_{\omega 2,e} \right\rangle \cdot \hat{z}}{-\left\langle \vec{S}_{\omega 1,e} \right\rangle \cdot \hat{z}} = \frac{\eta_2 \, |\eta_1|^2}{\eta_1 \, |\eta_2|^2} = \frac{\mathrm{sgn}(\eta_2)|\eta_1|}{\mathrm{sgn}(\eta_1)|\eta_2|} \tag{5}$$

Now consider the case in which both regions are nonmagnetic, i.e., they are dielectrics with $\mu_2 = \mu_1 = \mu_0$, μ_0 being the free-space permeability. Let Region 2 be free space with $\varepsilon_2 = \varepsilon_0$, ε_0 denoting the permittivity of free space. Let the permittivity of Region 1 be $\varepsilon_1 = \varepsilon_{r1}\varepsilon_0$. The index of refraction in Region 1 is thus $n_1 = \sqrt{\varepsilon_1 \, \mu_1} / \sqrt{\varepsilon_0 \, \mu_0} = |\varepsilon_{r1}|^{1/2}$ and Eq. (5) becomes:

$$\frac{\left\langle \vec{S}_{\omega 2,e} \right\rangle \cdot \hat{z}}{-\left\langle \vec{S}_{\omega 1,e} \right\rangle \cdot \hat{z}} = \frac{1}{|\varepsilon_{r1}|^{1/2}} = \frac{1}{|n_1|} \tag{6}$$

Thus, if the dielectric has a large permittivity (index of refraction), then a significant portion of the radiated power will reside in Region 1, the dielectric half space. For example, if $\varepsilon_{r1} = 11.7$, the ratio is 1/3.42 which means only 29.24% of the power is radiated into the free space region while 70.76 % of it is directed into the dielectric region. The situation is even more dire in three dimensions (3D). As predicted for an infinitesimal electric dipole on the interface in [18], the 3D ratio is

$$\frac{\left\langle \vec{S}_{\omega,e2} \right\rangle \cdot \hat{z}}{-\left\langle \vec{S}_{\omega,e1} \right\rangle \cdot \hat{z}} = \frac{1}{|\varepsilon_{r1}|^{3/2}} = \frac{1}{|n_1|^3} \tag{7}$$

The dual infinitesimal magnetic dipole case was considered in [19]. Consequently, the 3D ratio (7) for the silicon example is 1/40.0 which means 97.5% (2.5%) of the radiated power is emitted into the dielectric (air). Clearly, the large fields pointed away from the free-space region significantly impacts the performance characteristics of any antenna placed on the interface [1], [2], [4], [6], [7].

B. BALANCED ELECTRIC AND MAGNETIC CURRENT SHEETS ON AN AIR-DIELECTRIC INTERFACE

Now consider the combined canonical problem shown in Fig. 2. Both electric and magnetic current sheets are

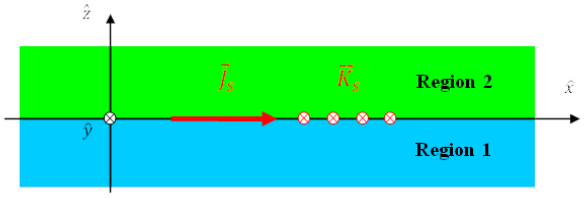

FIGURE 2. 1D analytical problem: Orthogonal infinite electric and magnetic current sheets on the interface between two 3D semi-infinite regions.

centered on the interface. As derived in the Appendix, the composite fields in Region 2 are:

$$\begin{aligned} \vec{E}_{\omega,\mathrm{total}\ 2} &= -\left(\frac{\eta_2}{\eta_1 + \eta_2} \right) \left[\, \eta_1 \, J_0 + K_0 \, \right] \, e^{-j k_2 z} \, \hat{x} \\ \vec{H}_{\omega,\mathrm{total}\ 2} &= -\left(\frac{1}{\eta_1 + \eta_2} \right) \left[\, \eta_1 \, J_0 + K_0 \, \right] \, e^{-j k_2 z} \, \hat{y} \end{aligned} \tag{8}$$

and in Region 1:

$$\begin{aligned} \vec{E}_{\omega,\mathrm{total}\ 1} &= -\left(\frac{\eta_1}{\eta_1 + \eta_2} \right) \left[\, \eta_2 \, J_0 - K_0 \, \right] \, e^{+j k_1 z} \, \hat{x} \\ \vec{H}_{\omega,\mathrm{total}\ 1} &= \left(\frac{1}{\eta_1 + \eta_2} \right) \left[\, \eta_2 \, J_0 - K_0 \, \right] \, e^{+j k_1 z} \, \hat{y} \end{aligned} \tag{9}$$

Then, as demonstrated in Appendix A, if the electric and magnetic currents are designed to be balanced so that $K_0 = \eta_2 \, J_0$, the total fields become Huygens fields, i.e.,

$$\begin{aligned} \vec{E}_{\omega 2,\mathrm{total}} &= -\eta_2 \, J_0 \, e^{-j k_2 z} \, \hat{x} \\ \vec{H}_{\omega 2,\mathrm{total}} &= -J_0 \, e^{-j k_2 z} \, \hat{y} \\ \vec{E}_{\omega 1,\mathrm{total}} &= 0 \\ \vec{H}_{\omega 1,\mathrm{total}} &= 0 \end{aligned} \tag{10}$$

Therefore, the corresponding total radiated power density in both regions is:

$$\begin{aligned} \left\langle \vec{S}_{\omega 2,\mathrm{total}} \right\rangle &= +\frac{1}{2} \, \eta_2 \, |J_0|^2 \, \hat{z} \\ \left\langle \vec{S}_{\omega 1,\mathrm{total}} \right\rangle &= 0 \end{aligned} \tag{11}$$

Thus, there is no power radiated into the dielectric, Region 1, and all the emitted power is radiated into free space, Region 2. This analytical Huygens source result gives credence to the hope that realistic 3D HDAs will provide a means to overcome the problems associated with antennas placed on the interface of a high permittivity dielectric.

Note from Eqs. (8) and (9) and as detailed in Appendix A that if the balanced source condition: $K_0 = -\eta_1 \, J_0$, were elected, the opposite would occur, i.e., then

$$\begin{aligned} \left\langle \vec{S}_{\omega 2,\mathrm{total}} \right\rangle &= 0 \\ \left\langle \vec{S}_{\omega 1,\mathrm{total}} \right\rangle &= -\frac{1}{2} \, \eta_1 \, |J_0|^2 \, \hat{z} \end{aligned} \tag{12}$$

Consequently, zero power would be radiated into free space, Region 2, and all the emitted power would be radiated into the

dielectric, Region 1. This result has other interesting implications. It means that a Huygens source could be custom-designed to emit completely into a dielectric body. Such a source would have immediate applications for the efficient generation of in-body waves associated, for instance, with medical imaging or hyperthermia cancer treatments because it would avoid the current standard need for bulky, lossy impedance matching layers. Similarly, it could also enhance ground penetrating radar (GPR) systems by concentrating most of their radiated power into the earth in search of buried unexploded ordnance or into concrete for non-destructive evaluation of rebar in bridge structures.

III. 3D PROBLEM AND IDEAL HUYGENS DIPOLE SOURCE SOLUTION

Ideal electrically small electric and magnetic dipole antennas are introduced to bridge the gap between the canonical and realistic 3D structures. Basic center-fed dipoles act as the electric radiators. Small loop antennas act as the magnetic dipoles [20]. Both idealized dipole antennas are driven with voltage sources (lumped ports) having specified input impedance values that yield a minimum reflection coefficient at the target frequency. The following results clearly demonstrate that the appealing analytical outcomes persist for finite 3D sources and structures. These ideal results will then be extended to more realistic configurations in the next section.

With no lack of generality, all of the reported simulation results target $f_0 = 300$ MHz as the source frequency to yield a free space wavelength $\lambda_0 = 1000$ mm. This choice allows for a quick grasp of all lengths in terms of a wavelength and facilitates the opportunity to apply the HDA design reported in [15] directly to the final stages of this exploratory work. The materials considered herein would not begin to exhibit significant dispersion properties until well into the terahertz regime. The final NFRP HDA designs are scalable to higher frequencies, e.g., [16], [17], [21].

The electric and magnetic radiators and their Huygens source combinations will be placed on the interface of a thick, high permittivity, finite-sized dielectric block. This dielectric block was selected in all cases to have bulk parameters the same as the Rogers RT/Duroid 6010 laminate material, i.e., a relative permittivity of 10.2, a relative permeability of 1.0, and a loss tangent of 0.0023. This choice rather than silicon ($\varepsilon_r = 11.7$) was made in anticipation of the fabrication of prototypes of the final designs and their testing at X-band frequencies in the measurement chamber that is locally available. The size of the block was assumed simply to be large with respect to the electrically small antennas considered, i.e., its dimension are $0.5\lambda_0 \times 0.5\lambda_0 \times 0.3\lambda_0 = 500 \times 500 \times 300\,\text{mm}^3$. The block is considerably larger when the wavelength in the block is taken into account, i.e., $\lambda_0 = 3.2\,\lambda_{\text{block}}$. The lengths of its sides in terms of λ_{block} thus do not support any corresponding half-wavelength resonances in it. The normal to the top face of the block is always specified to be pointed along the +z-axis. All of the two-dimensional (2D) directivity plots presented throughout have the same

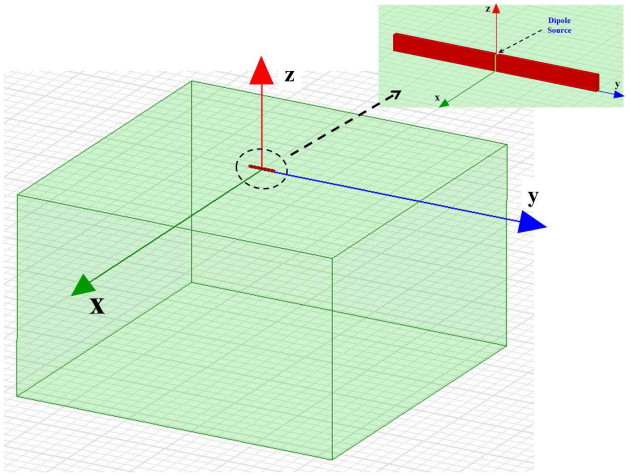

FIGURE 3. 3D problem: Electrically small center-fed dipole antenna centered on the interface between free space and a finite-sized high permittivity block.

dB scale, −20 to +10 dB, for ease of comparison. Moreover, all of these directivity patterns have markers labeled $m1$ and $m2$ to indicate the directivity value for $\theta = 0°$ (+z-axis) and $\theta = 180°$ (-z-axis), respectively.

A. ELECTRIC DIPOLE

As with the canonical analytical results, the reference case for the ideal studies is an electric dipole placed on the surface of the block as shown in Fig. 3. It has a total length of $\lambda_0/25$ (40.0 mm) and is oriented along and centered on the y-axis. It is electrically small with $ka = 0.25 < 1$, where $ka = 2\pi a/\lambda_0$ and $a = 20.0$ mm is the radius of the smallest enclosing sphere. It has a 3.0 mm width (along the z-axis) and is 1.0 mm thick (along the x-axis). The driving voltage source is located in a gap at its center, i.e., it is a center-fed dipole. Clearly, it is more than an order of magnitude smaller than the physical size of the block. This size contrast incurred large simulation times. Thus, the dipole material was specified to be a perfect electric conductor (PEC) to simplify the simulations of the idealized dipoles.

This dipole antenna was simulated first in free space for comparison purposes. As indicated in Fig. 4, it has a simulated maximum directivity $m1 = 1.36$ dB (1.37), just below the theoretical maximum for such a small dipole radiator, 1.64 dB (1.5). The simulated 2D directivity pattern with respect to θ for $\phi = 90°$, i.e., the yz-plane pattern, has the well-known doughnut shape since that plane contains the dipole [20]. It is omnidirectional in the $\phi = 0°$ plane, i.e., the zx-plane, orthogonal to the dipole. Since $m2 = 1.36$ dB, its front-to-back ratio ($FTBR$) in both planes is $m1/m2 = 0$ dB (1.0).

The simulated 2D directivity patterns of the same dipole on the dielectric block are shown in Fig. 5. It is clearly seen that the radiated power is directed mainly into the dielectric as expected. The maximum directivity, $m2 = 5.67$ dB, is along the -z-axis. The directivity in the opposite direction is $m1 = 0.50$ dB. Consequently, the $FTBR$ value relative to

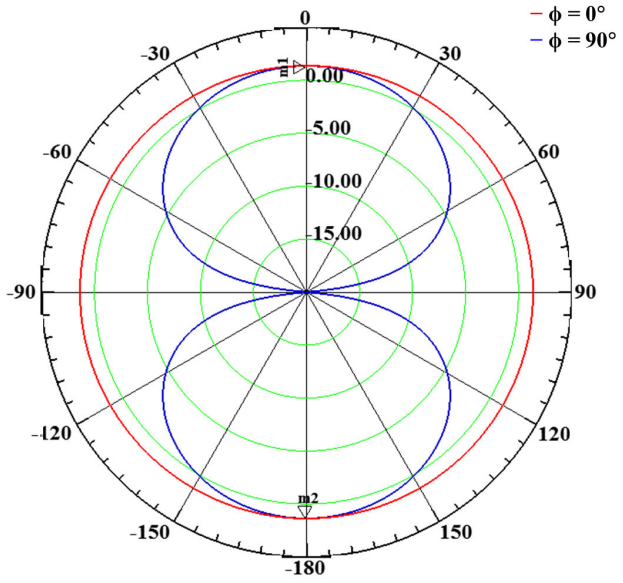

FIGURE 4. Simulated 2D directivity patterns of the electrically small, electric dipole antenna radiating in free space at f_0.

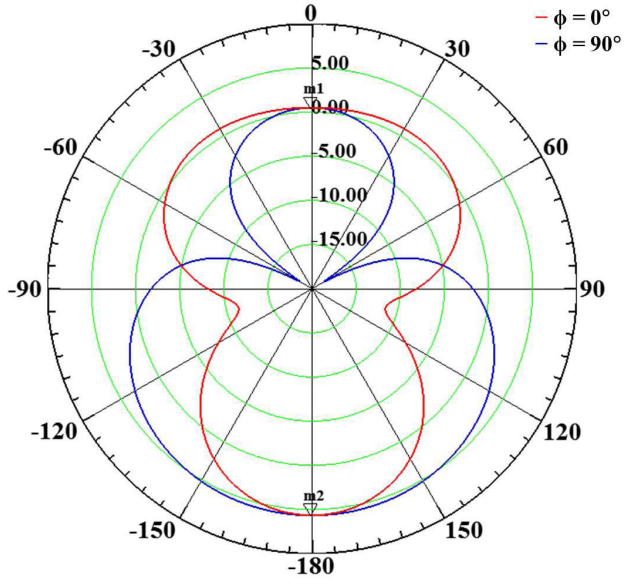

FIGURE 5. Simulated 2D directivity patterns at f_0 of the electrically small, electric dipole antenna centered on the high permittivity block.

the maximum direction (into the block) is 5.17 dB. Moreover, comparing these patterns to those of the dipole in free space, one observes immediately that the dielectric block causes more power to be maximally directed into it. Furthermore, the presence of the block significantly alters that dipole's omnidirectional feature. While the maximum directivity in both principal planes is the same and directed into the block, the pattern in the *yz*-plane in which the dipole lies is much smaller in the air region and much larger and broader in the high permittivity region.

The polarization currents induced in the *yz*-plane reinforce the power radiated into the block and weaken the power radiated into the air region. Despite the wavelength in the

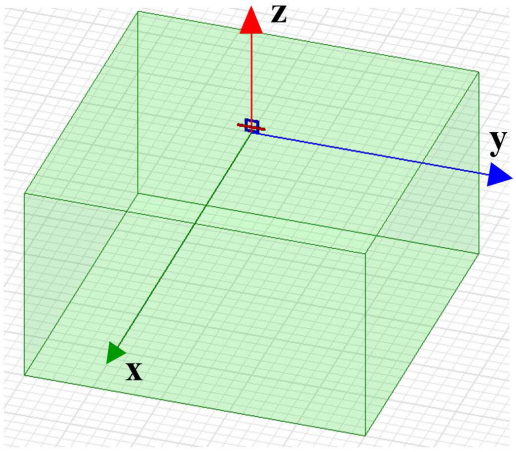

(a) Isometric view

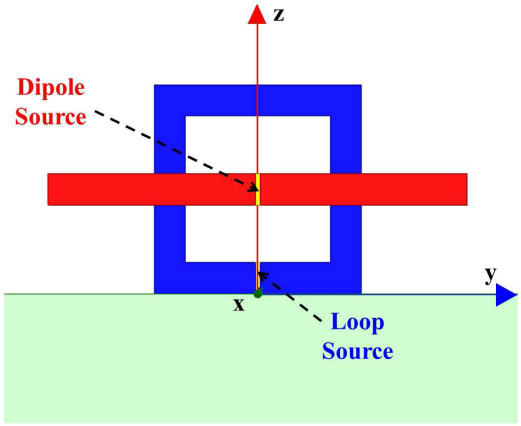

(b) Side view of the array

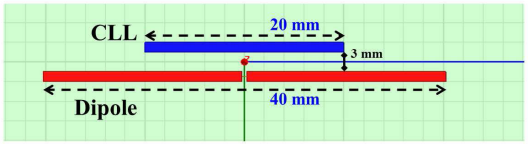

(c) Top view of the array

FIGURE 6. 3D problem: Electrically small Huygens electric and magnetic dipole array centered on the high permittivity block.

medium being smaller than in free-space, the dipole along the y-axis is still electrically small. Consequently, the beam width in Region 1 is broad. On the other hand, the dipole remains very thin in the *zx*-plane. Consequently, there are much weaker polarization currents induced by it. While they nevertheless cause the pattern to lose its omnidirectional form and much of the radiated power is still directed into the block, they have much less impact on the portion of the pattern in the air region. Thus, the overall power radiated into the free space region is larger and is also broader since the dipole is smaller as seen from Region 2 than from Region 1.

B. COMBINED ELECTRIC AND MAGNETIC IDEAL DIPOLES

Now consider the Huygens configuration shown in Fig. 6. This electric and magnetic dipole array is a simple

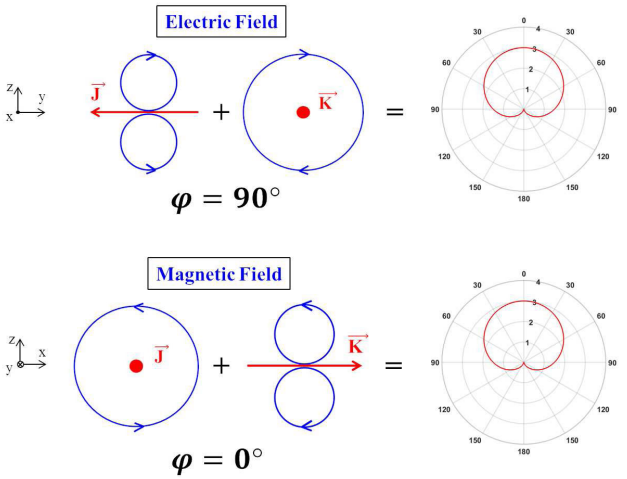

FIGURE 7. The Huygens radiation physics of a pair of balanced, in-phase, orthogonally oriented, infinitesimal electric and magnetic dipoles in free space.

combination of a dipole and a loop element; it is centered on the top face of the block. The simulation studies of the magnetic dipole (loop) antennas considered in the following discussions are detailed in Appendix B.

The electric element is the same center-fed dipole discussed above. As illustrated in Fig. 6(b), the magnetic element is a square loop with a 20 mm side length ($ka = 0.089$) that is centered on the top face of the block along the y-axis. The loop is oriented orthogonal to that face. The width of each of its strips (along the y and z axes) is 3.0 mm and their thickness (along the x-axis) is 1.0 mm. The loop is also taken to be a PEC to simplify the simulations. It is driven by a voltage source located in a gap at the center of its side on the interface. This position gives the best radiated power outcome away from the block (see Appendix B). As illustrated in Fig. 6(c), the loop and the dipole are separated by 3.0 mm.

Following the operational mechanisms learned in [15], the phase centers of both dipoles were arranged to coincide to achieve the best Huygens pattern. As illustrated in Fig. 6(b), the center of the electric dipole was positioned vertically to be the same as the center of the loop, 10.0 mm above the interface. The signs of both voltage sources were selected to have the maximum of the resulting broadside pattern point along the +z-axis. In particular, the electric current moment points along the -y-direction. The loop current flows in a counterclockwise sense relative to looking at the loop from the +x-axis towards the origin. This loop current direction creates a magnetic current moment pointed along the +x-direction. The electric and magnetic fields radiated by these electric and magnetic currents yield the broadside field pointed along the +z-axis as illustrated in Fig. 7 [22]. Moreover, because the electric and magnetic dipoles are located very near to each other, they are tightly coupled. Hence, their input impedances were adjusted to have negligible reflection coefficients near the targeted source frequency f_0.

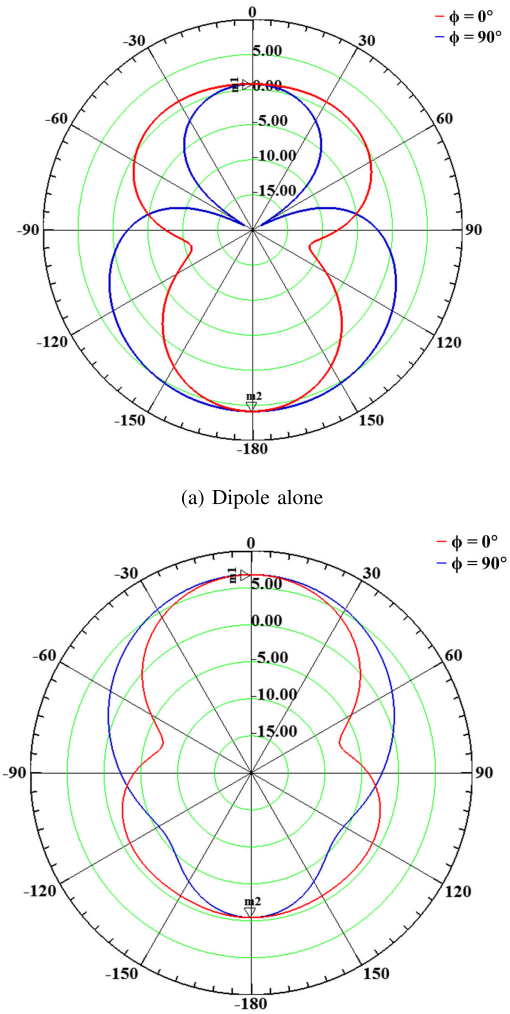

(a) Dipole alone

(b) Loop alone

FIGURE 8. Simulated 2D directivity patterns at f_0 of the individual elements of the electrically small Huygens dipole array.

The simulated 2D directivity patterns at f_0 of the these electric and magnetic dipoles as individual radiators in the presence of the high permittivity block are shown in Fig. 8. The power radiated by the electric dipole displaced from the interface remains mainly directed into the block. The directivity markers $m1 = 0.80$ dB and $m2 = 5.86$ dB, which are very similar values to those noted for the dipole directly residing on the block. The height of this dipole above the interface had only a very minor impact on its performance characteristics. On the other hand, the power radiated by the loop has significantly more power radiated into the free space region. The directivity markers $m1 = 6.78$ dB and $m2 = -0.44$ dB demonstrate that the magnetic dipole is a superior choice over an electric one on a high permittivity block. Nonetheless, there is clearly non-trivial power radiated into the back direction and only a modest $FTBR = 7.22$ dB is attained.

The simulated 2D directivity patterns at f_0 of this Huygens two-element dipole array in free space are given in Fig. 9a.

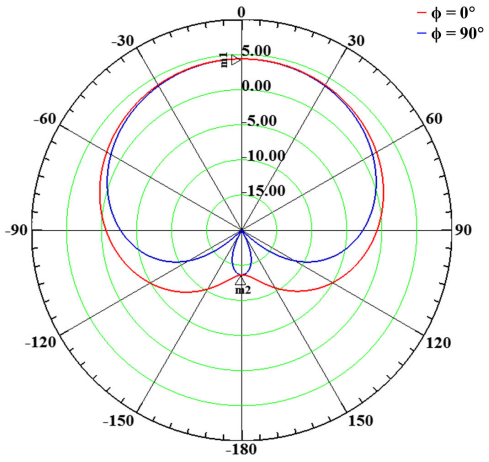

(a) Free space

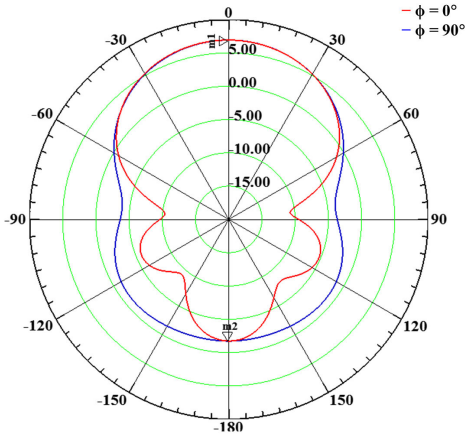

(b) Centered on the high permittivity block with equal source weighting

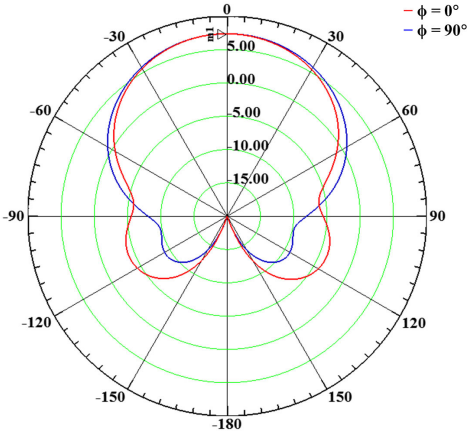

(c) Centered on the high permittivity block with optimized source weighting

FIGURE 9. Simulated 2D directivity patterns at f_0 for the electrically small Huygens dipole array.

The input power to both dipole elements is the same. The cardioid pattern that is characteristic of Huygens sources is very apparent. The maximum directivity in this case is $m1 = 4.38$ dB along the +z-axis. This value is near to the maximum directivity associated with an infinitesimal HDA, 4.77 dB (3.0). The opposite directivity $m2 = -13.62$ dB. It is quite small as it would be for an infinitesimal Huygens dipole antenna. The resulting $FTBR = 18.0$ dB.

The simulated 2D directivity patterns at f_0 of this Huygens two-element dipole array centered on the interface of the block are given in Figs. 9b and 9c. These directivity patterns are clearly pointed primarily away from the block into free space in the direction broadside to the radiating elements. Moreover, there is clearly little back-radiated field. However, the sources of the radiating elements in these two cases are different.

The patterns in Fig. 9b were generated with both elements having the same input power as in the free space case. The maximum directivity is $m1 = 6.92$ dB along the +z-axis and is $m2 = -1.74$ in the opposite direction. These values yield the $FTBR = 8.66$. The performance is somewhat improved over the magnetic dipole alone, but the anticipated cardioid pattern was not attained. The cancellation of the back-radiated fields is weak.

Investigating further, it was found that the electric dipole produces fields in the dielectric along the -z-direction that are about twice the magnitude of those generated by the loop. Consequently, it was decided to feed the loop with twice the input power that is used to drive the electric dipole in order to achieve the best cancellation of the back-radiated broadside fields. Moreover, the strong polarization currents induced by the electric dipole impact the relative phases of both radiating elements. It was determined that magnetic dipole source required a $+\pi/4$ phase difference with respect to that of the electric one to achieve the optimized patterns. It will be seen in the next section that with more complicated, realistic radiating elements, a similar optimization of the balance between the electric and magnetic radiators is necessary and accomplished primarily by adjusting the height of the electric element relative to the interface (and, hence, relative to the polarization currents it induces in the dielectric) and the phase center of the magnetic one.

The directivity patterns in Figs. 9c were generated with this optimized balanced weighting of the electric and magnetic elements. The cardioid pattern is clearly visible. The maximum directivity is $m1 = 7.37$ dB along the +z-axis, which is nearly 3 dB larger than the free space case as a consequence of that weighting. The directivity value along the -z-axis was too small for the software to generate a marker in the proper location with the specified scale. Nevertheless, the calculated $FTBR = 39.14$ dB (8210.3). The quality of the patterns with the optimized weighting of the elements validates the expectations from the canonical results.

It should be noticed that the maximum value of the directivity generated by the magnetic element itself on the block is quite large. On the other hand, it is also quite clear that the balanced weighting of the dipole array does significantly improve the cancellation of the back-radiated fields of that case. Moreover, it improves the beamwidth of the patterns in the free-space region, i.e., much of the additional input power is radiated into a broader range of angles. Nevertheless,

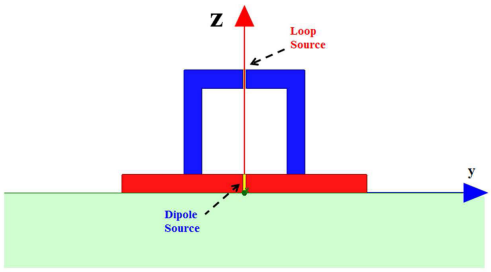

(a) Configuration

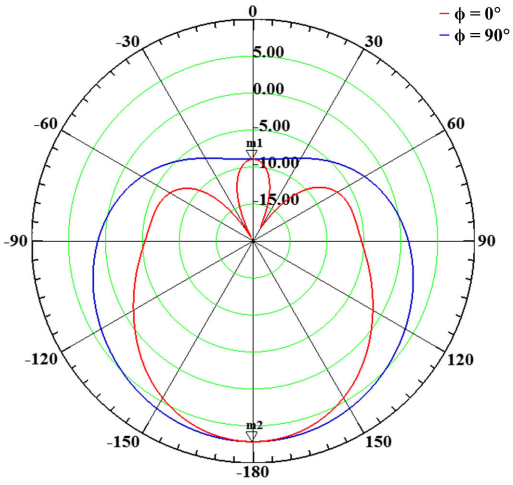

(b) Simulated 2D directivity patterns at f_0

FIGURE 10. **Huygens dipole pair centered on the high permittivity block that is purposely designed to radiate into it.**

in comparing the free space and block directivity patterns, one notes that their cardioid shape is more directive in the block case and are not nearly as wide-angled as they are in the free space case. This feature is consistent with the presence of the strong polarization currents induced in the block by the Huygens dipole pair. It is clear that the broadside forward and back radiation performance characteristics of the optimized Huygens dipole array in the presence of the block is vastly superior to those associated with corresponding dipole alone and exceeds that of the loop alone.

Finally, the other possibility that one could custom design a Huygens source that radiates primarily into the high permittivity block was explored. Following the analysis in [15], the current in one of the two radiators had to be reversed and their relative phase center positions had to be changed to optimize the power radiated into the block. The best configuration was determined to be the one in which both the electric dipole and the loop are in contact with the interface and in which the choice is made to have the source of the loop centered in its top segment. It is shown in Fig. 10a. As demonstrated in Section III.A, an electric dipole lying directly on the interface naturally radiates most of its power into the block. On the other hand, while the bottom-source loop directs a majority of its power into free space, the top-source loop does the opposite (see Appendix B). The simulated 2D directivity patterns at f_0 of this Huygens dipole array centered on the interface of the block and excited with the same optimized balanced weighting of their sources employed in the air-region emphasized case are given in Fig. 10b. Here, the optimized source weighting of the magnetic dipole again produces the desired cancellation of the back-radiated fields, which now occurs in the air region. A slightly distorted cardioid pattern is achieved whose more narrow beamwidth is directed into the block. The stronger induced polarization currents help to directly channel the radiated power into it. The maximum directivity $m2 = 7.13$ dB is along the -z-axis. The directivity in the opposite (air) direction is $m1 = -8.95$ dB. The $FTBR = 16.08$ dB. As desired, a majority of the radiated power is directed into the block by design. These results confirm the more general possibility for customed-designed HDAs that can direct their radiated power either into or away from more complex media.

IV. REALISTIC HUYGENS DIPOLE ANTENNA RESULTS

The electrically small Huygens dipole antenna developed in [15] was modified to explore if an actual system could achieve behaviors similar to the corresponding idealized Huygens dipole array when it is centered on the surface of the high permittivity block. The original design consisted of a coax-fed dipole that drives three NFRP elements, one electric Egyptian axe dipole (EAD) element and two magnetic capacitively loaded loop (CLL) elements. A variant that is matched to a 50-Ω lumped source in free space and on the block is reported first as it is closely connected to the ideal cases. A second variation which includes a coax feed structure that is embedded in the dielectric block is considered next. The embedded structure mimics an internal source so that the antenna acts as a radiator. Considering the same antenna as a receiver, it could also be interpreted as a shielded region in which it is matched to a load such as a wirelessly powered sensor [23] or communications system [24]. Real material properties were used for all of the antenna components in the simulated results reported in this section.

A. DIPOLE REFERENCE CASE

A center-fed electric dipole antenna similar to the one in the first HDA design was simulated for reference purposes. The geometry is shown in Fig. 11a. Here, the dipole is formed as two copper strips printed and centered on the dielectric block. A lumped port drives the antenna and its input impedance was specified to give complete matching at the source frequency and, hence, the best possible performance. Its total length is 0.114 λ_0, 114 mm. Its half-length is the same as the radius of the EAD elements employed in the HDA designs. It is 2.0 mm wide and 0.017 mm thick. The block, of course, is the same as in all of the previous cases. The simulated 2D directivity patterns are shown in Fig. 11b. The patterns are pointed primarily into the block as expected and have forms immediately recognizable from those reported for the ideal dipole. The maximum directivity into the block $m2 = 5.83$ dB

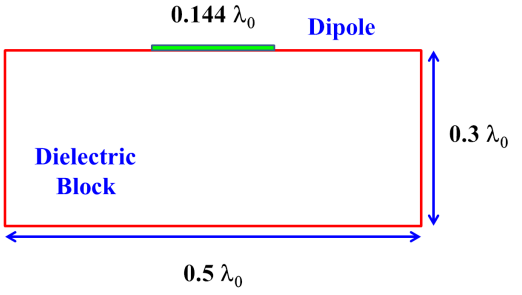

(a) Configuration

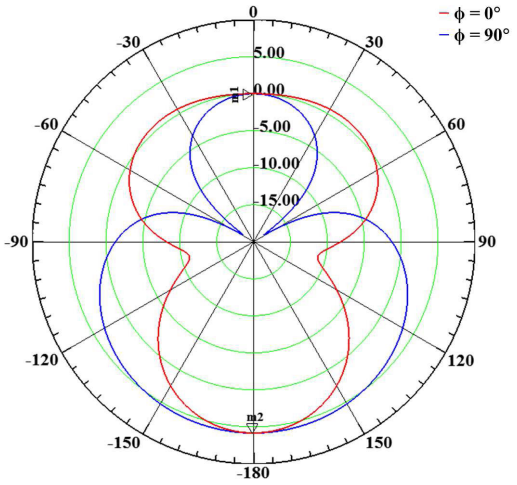

(b) Simulated 2D directivity patterns at f_0

FIGURE 11. Electrically small, center-fed, printed electric dipole antenna centered on the high permittivity block.

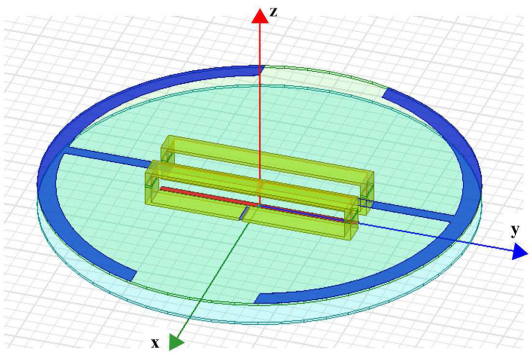

(a) HDA in free space

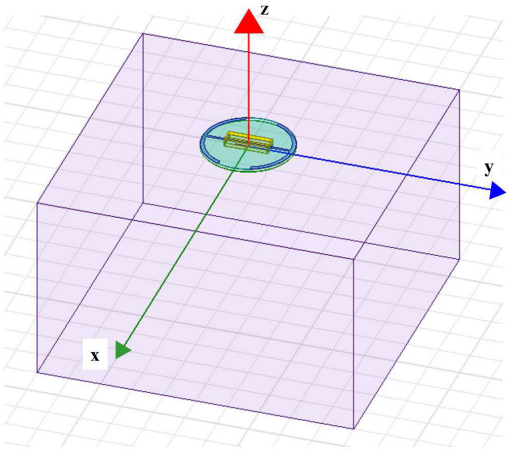

(b) HDA on the high permittivity block

FIGURE 12. Electrically small Huygens dipole antennas: 3D perspective views.

and the directivity in the opposite direction into free space $m1 = 0.00$ dB. Thus, the ratio is 5.83 dB.

B. HDA MATCHED TO A 50-Ω LUMPED SOURCE ON THE BLOCK

A 3D perspective view of the custom-designed HDAs that are matched to a 50-Ω lumped element source in the simulation model are shown in Figs. 12(a) and 12(b), respectively. The corresponding 2D top view and the side views in free space and on the block are shown in Figs. 13 (a)-(c). These metamaterial-inspired, linearly polarized, NFRP antennas combine a driven printed dipole with a balanced set of EAD and CLL NFRP elements.

In all cases presented in this and the next subsection, the radius of the entire antenna system is the radius of the EAD element, $\text{EAD}_{\text{radius}} = 72.0$ mm ($\lambda_0/13.89$). Both substrates are circular disks whose radii are the same as the EAD element's. They are both taken to be 0.7874 mm thick Rogers RT/Duroid 5880 board material with $\varepsilon_r = 2.2$, $\mu_r = 1.0$ and $\tan\delta = 0.0009$ and 0.5 oz (0.017 mm thick) copper. The dipole is printed on the bottom face of the lower disk. In the block cases it lies directly on the interface. The width of this printed dipole is 2.0 mm. The EAD element lies on the top of the upper substrate. As with the original HDA design [15], a single inductor with inductance L is introduced at the center of the EAD element's straight segment. It facilitates resonance frequency tuning of the EAD element [15], [25]. The width of the center strip of the EAD is $\text{EAD}_{\text{center width}} = 4.0$ mm. The CLL elements rest on top of the bottom substrate and penetrate through the upper substrate. Their length, height and width are, respectively, $\text{CLL}_{\text{length}} = 70.0$ mm, $\text{CLL}_{\text{height}} = 10.0$ mm and $\text{CLL}_{\text{width}} = 8.0$ mm. The distance between the centerline of the dipole and the inside edges of the CLL elements is 8.0 mm. Each CLL element has a capacitor with capacitance C integrated into it; the center of the capacitor is offset by -2.5 mm along the y-axis from the center of the CLL. They facilitate resonance frequency tuning of the CLL elements [15], [25]. The voltage source and the lumped elements are introduced in the simulation model, respectively, as a lumped excitation source and as *RLC* sheet elements across 1.0 mm gaps in the copper strips in which they lie. Their widths match those of the copper strips and are centered vertically in those gaps. The EAD parameters: $\text{EAD}_{\text{arc width}}$ and EAD_{gap} and the dipole length $\text{Dipole}_{\text{length}}$ are varied to achieve fine tuning of the input impedance and facilitate matching to the source. The distance between the upper

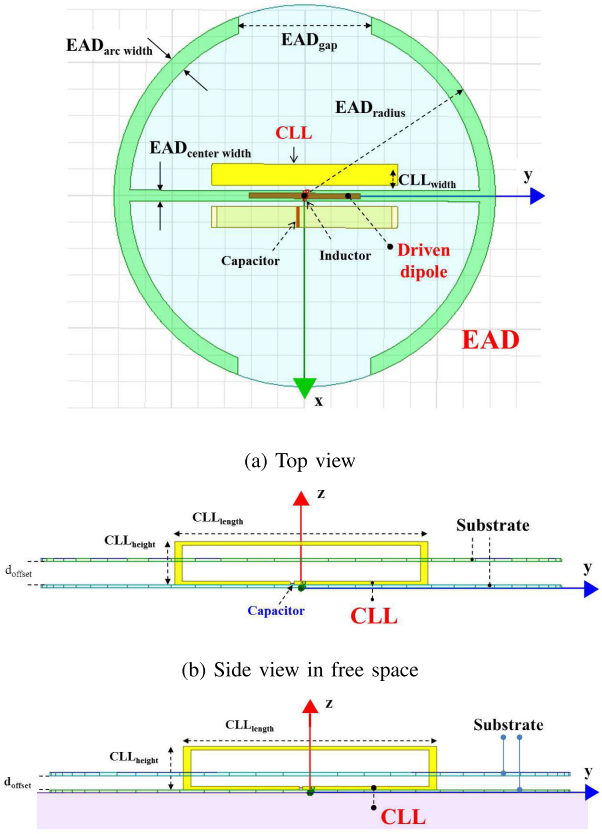

(a) Top view

(b) Side view in free space

(c) Side view on the high permittivity block

FIGURE 13. 2D views of the HDAs and the design parameters.

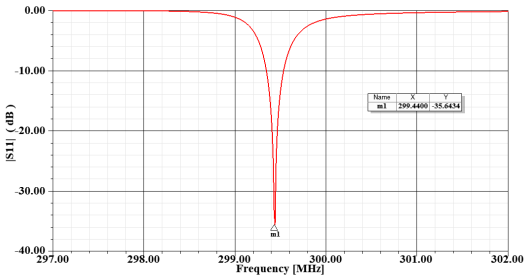

(a) $|S_{11}|$ values versus frequency

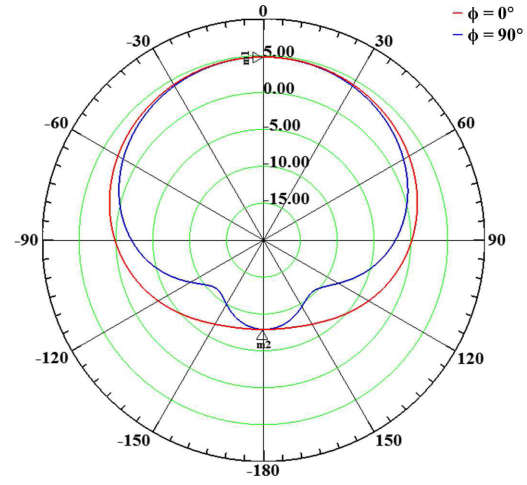

(b) Simulated 2D directivity patterns at f_{res}

FIGURE 14. Electrically small Huygens dipole antenna matched to a 50-Ω lumped source radiating in free space.

surface of the lower substrate and the lower surface of the upper substrate is d_{offset}. It is adjusted to optimize the Huygens behavior pointing along the +z-axis [15].

The parameters in the free space case are: $\text{EAD}_{\text{arc width}} = 6.0$ mm and $\text{EAD}_{\text{gap}} = 42.0$ mm $L = 56.0$ nH, $C = 5.0$ pF, $\text{Dipole}_{\text{length}} = 67.3$ mm, and $d_{\text{offset}} = 7.28$ mm. The simulated performance characteristics are presented in Fig. 14. The $|S_{11}|$ values in Fig. 14(a) indicate that its minimum reflection coefficient, -35.64 dB, with respect to the 50-Ω source occurs at $f_{res} = 299.436$ MHz. With this resonance frequency and the height of the second substrate, one finds $ka = 0.45$. The 2D directivity patterns at the resonance frequency in the principal planes are given in Fig. 14(b). The desired cardioid shapes with their maximum along the z-axis were attained. The directivity marker values $m1 = 4.82$ dB and $m2 = -7.90$ dB give $FTBR = 12.72$ dB. The radiation efficiency is 88.02%.

The parameters in the block case are: $\text{EAD}_{\text{arc width}} = 6.0$ mm and $\text{EAD}_{\text{gap}} = 50.0$ mm $L = 0.1$ nH, $C = 3.9$ pF, $\text{Dipole}_{\text{length}} = 42.0$ mm, and $d_{\text{offset}} = 4.70$ mm. The simulated performance characteristics are presented in Fig. 15. The $|S_{11}|$ values in Fig. 15(a) indicate that its minimum reflection coefficient, -31.16 dB, with respect to the 50-Ω source occurs at $f_{res} = 302.313$ MHz. With this resonance frequency and the height of the second substrate, one finds $ka = 0.46$. The 2D directivity patterns at the resonance frequency in the principal planes are given in Fig. 15(b). The directivity markers $m1 = 7.18$ dB and $m2 = -32.11$ dB along the z-axis give $FTBR = 39.29$ dB. The radiation efficiency is 81.23%.

As illustrated in Figs. 13(b) and 13(c), the height of the EAD element had to be adjusted substantially closer to the dielectric interface to achieve the optimal Huygens behavior. In analogy with the ideal Huygens dipole array case, this adjustment is necessary because the presence of the polarization currents in the block changes the relative phase centers of the radiating NFRP elements. If the EAD height is not lowered, the electric and magnetic dipole pair radiates primarily into the block. Furthermore, the presence of the two CLL elements doubles the magnetic dipole strength and, hence, the amplitude of the fields radiated by them into the block. This leads to the effective cancellation of the back radiation as it did in the ideal case. As Fig. 15(b) clearly illustrates, this custom-designed HDA is radiating a significant portion of its radiated power into the free-space region.

C. COAX-FED HDA ON THE BLOCK

To address the issue of the impact of an actual feed structure on the outcomes, the HDA was custom-designed again to be

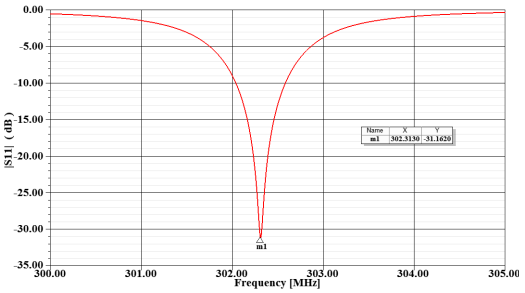

(a) $|S_{11}|$ values versus frequency

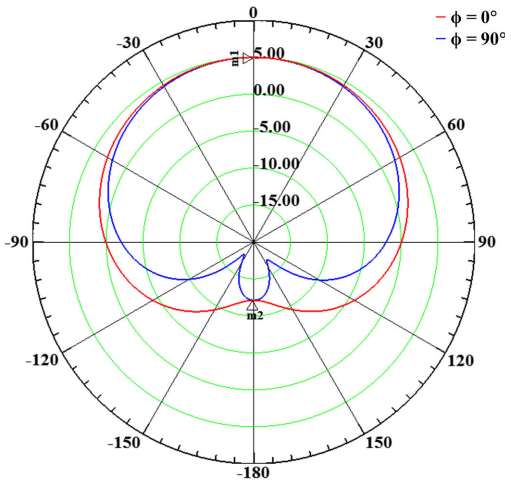

(b) Simulated 2D directivity patterns at f_{res}

FIGURE 15. Electrically small Huygens dipole antenna matched to a 50-Ω lumped source and centered on the high permittivity block.

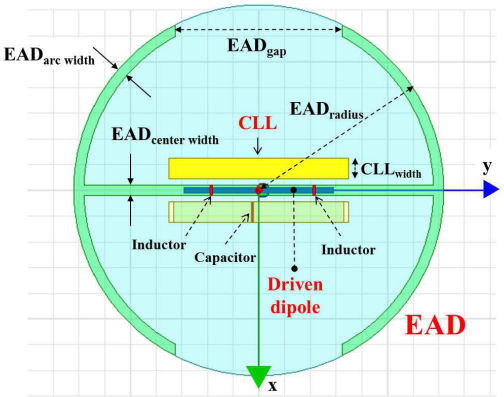

(a) Top view

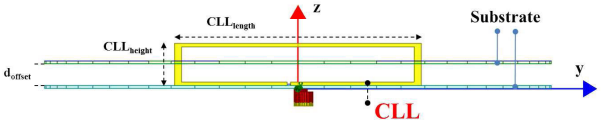

(b) Side view in free space

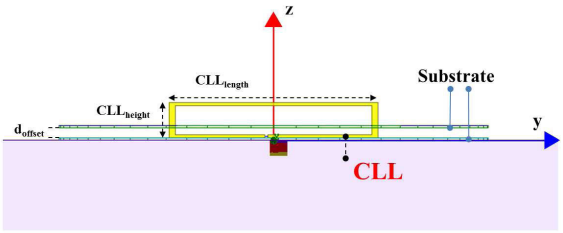

(c) Side view on slab

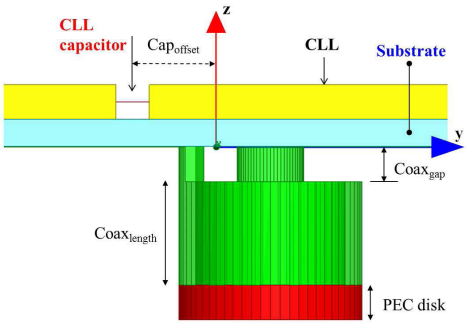

(d) Zoom-in on coax feed

FIGURE 16. 2D views of the coax-fed HDAs and the additional design parameters.

coax-fed from a 50-Ω source when it is in free space and when it lies on the dielectric block with the coax feed embedded in it. The 2D top view and the side views in free space and on the block are shown in Figs. 16 (a)-(c). A close-up of the coax feed is shown in Fig. 16(d). In contrast to the HDA design in the previous subection, two inductors are placed symmetrically away from the source region in the center strip of the EAD. The offset distance to the center of the inductors in both designs is 20 mm. This choice was purposely made to move the inductors away from the feed region and to illustrate further the flexibility of the design. Moreover, given the narrow bandwidth of the HDA designs, this version would allow non-Foster elements to be incorporated into the EAD element in a more symmetrical manner than the layout in the original non-Foster augmented prototypes [26], [27].

The coax is air filled. The radius of its center conductor is 1.0 mm and the thickness of its outer wall is 0.5 mm. The ratio of the inner radius of its outside wall to the center conductor radius is set to 2.238 to attain the 50-Ω wave impedance. The coax length $\text{Coax}_{\text{length}} = 3.0$ mm; the distance between the end of the coax and the dipole is $\text{Coax}_{\text{gap}} = 1.0$ mm. The offset distance of the capacitors is again $\text{Cap}_{\text{offset}} = -2.5$ mm. A 50-Ω wave port is introduced at the bottom of the coax. A perfect electric conducting (PEC) disk is placed behind the wave port as necessitated by the software; its height is $PEC_{\text{disk}} = 1.0$ mm.

The parameters in the free space case are: $\text{EAD}_{\text{arc width}} = 6.0$ mm and $\text{EAD}_{\text{gap}} = 42.0$ mm $L = 30.5$ nH, $C = 5.0$ pF, $\text{Dipole}_{\text{length}} = 90.0$ mm, and $d_{\text{offset}} = 6.92$ mm. The simulated performance characteristics are presented in Fig. 17.

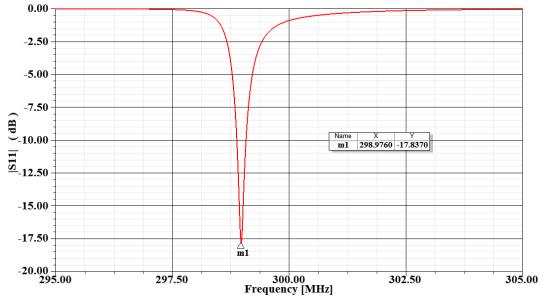

(a) $|S_{11}|$ values versus frequency

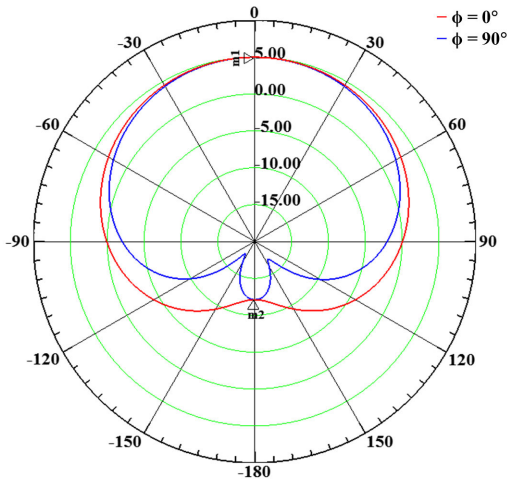

(b) Simulated 2D directivity patterns at f_{res}

FIGURE 17. Electrically small coax-fed Huygens dipole antenna radiating in free space.

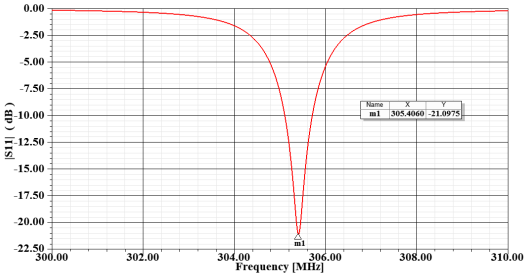

(a) $|S_{11}|$ values versus frequency

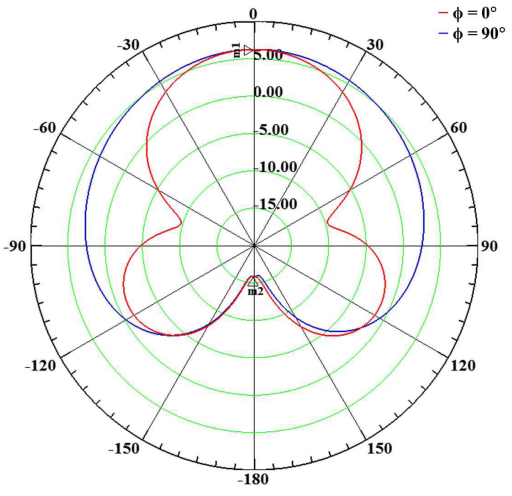

(b) Simulated 2D directivity patterns at f_{res}

FIGURE 18. Electrically small coax-fed Huygens dipole antenna centered on the high permittivity block.

The $|S_{11}|$ values in Fig. 17(a) indicate that its minimum reflection coefficient, -17.84 dB, with respect to the 50-Ω source occurs at $f_{res} = 298.976$ MHz. With this resonance frequency and the height of the second substrate, one finds $ka = 0.45$. The 2D directivity patterns at the resonance frequency in the principal planes are given in Fig. 17(b). The desired cardioid shapes with their maxima along the +z-axis were attained. The directivity markers $m1 = 4.98$ dB and $m2 = -12.11$ dB give $FTBR = 17.09$ dB. The radiation efficiency is 88.02%.

The parameters in the block case are: $\text{EAD}_{\text{arc width}} = 4.0$ mm and $\text{EAD}_{\text{gap}} = 65.0$ mm $L = 0.1$ nH, $C = 3.75$ pF, $\text{Dipole}_{\text{length}} = 58.0$ mm, and $d_{\text{offset}} = 4.30$ mm. The simulated performance characteristics are presented in Fig. 18. The $|S_{11}|$ values in Fig. 18(a) indicate that its minimum reflection coefficient, -31.16 dB, with respect to the 50-Ω source occurs at $f_{res} = 305.406$ MHz. With this resonance frequency and the height of the second substrate, one finds $ka = 0.46$. The 2D directivity patterns at the resonance frequency in the principal planes are given in Fig. 18(b). The directivity markers $m1 = 6.22$ dB and $m2 = -15.87$ dB along the z-axis give $FTBR = 22.09$ dB. The radiation efficiency is 81.75%.

As again illustrated by comparing Figs. 16(b) and 16(c), the height of the EAD element had to be adjusted substantially closer to the dielectric interface than in the free-space case to achieve the optimal Huygens behavior. Clearly, this custom-designed coax-fed HDA is also radiating a significant portion of the radiated power into the free-space region. Moreover, because the back radiation into the block is substantially lower than the coax-driven magnetic dipole alone (see Appendix C), the HDA system provides unique performance characteristics not obtained with either of its component elements alone. These results clearly demonstrate that the HDA design can be modified appropriately to accommodate the presence of the feed structure to attain this desired outcome.

D. DISCUSSION

Whether in free space or on the dielectric slab, the reported custom-designed HDA systems are admittedly narrow band, i.e., on the order of 1% fractional bandwidth. This is not an issue as receivers for wirelessly powered sensors since they would be optimized for the source frequency. On the other hand, the presence of the inductor and capacitors enable a frequency agile performance and a means to increase the bandwidth by augmenting the NFRP elements with embedded non-Foster circuits [25]–[28]. This frequency agility gives flexibility to the HDA when it is coupled with a communications device. Moreover, when integrated with, for example,

a sensor, it can be custom-designed to be directly matched to the impedance of the sensor at a targeted frequency [23]. On the other hand, the augmentation of the NFRP elements with non-Foster circuits substantially increases their bandwidths, typically by a factor of 10. They would then be adaptable to some broader bandwidth communications applications. Nevertheless, a dual functional WPT and communications HDA has been demonstrated even without the non-Foster augmentation [24].

The achieved radiation efficiencies are quite high and are inline with those previously demonstrated with measured HDA prototypes [23]–[29]. In anticipation for an actual experiment at RF or lower millimeter wave (mm-wave) frequencies, the high permittivity material was selected to be a well-known low loss copper-cladded board material. However, to achieve a HDA for mm-wave applications on silicon or other semi-conductor substrates, the HDA should be redesigned for the stack-up layouts associated with any potential CMOS type of fabrication technology and the foundry specific rules dictated by them. The design is simple in that it only requires four vias, printed copper strips, and dielectric layers. Moreover, one would want to embedded the HDA into the substrate for the most integrated OCA design rather than having it reside on the substrate. This objective is currently being pursued. On the other hand, the reported designs are ideal candidates for wearable and other systems intended to reside on a human body for off-body wireless connectivity. Furthermore, because their sizes are quite electrically small, the narrow bandwidths of the passive HDAs presented herein are inherent. However, as noted at the start, the physical sizes of even half-wavelength antennas for IoT and associated 5G systems in the 60 GHz (57-71 GHz) V band and other portions of the E (60-90 GHz) and D (110-170 GHz) bands will already be physically small. Scaling the presented efficient HDA designs to half-wavelength sizes would naturally lead to Huygens-based systems with substantially larger bandwidths that could be custom-designed to preferentially radiate away from or into a high permittivity region.

V. CONCLUSION

A possible approach to resolve a long standing problem associated with OCAs as the last bottleneck for achieving universally attractive wireless SoC solutions, as well as for wireless devices placed on a human body or other high permittivity dielectrics, was presented. It was demonstrated analytically with infinite current sheets on the interface between free space and a high permittivity dielectric half space that a Huygens arrangement of a balanced pair of in-phase orthogonal electric and magnetic sources would radiate primarily into free space rather than into the dielectric. This feature was then confirmed numerically to persist in several 3D configurations.

A driven, optimally balanced pair of ideal electrically small electric and magnetic dipole antennas was placed on the interface between free space and a high permittivity finite-sized block and their field behaviors were explored. The performance of the electric and magnetic radiators was evaluated separately and jointly. The anticipated radiation physics was verified; the ideal two element Huygens array could be designed to radiate primarily into free space. On the other hand, the array was modified by optimizing the relative position of the electric dipole with respect to the magnetic one to also demonstrate that one could, by choice, have the pair radiate preferentially into the dielectric block with little back radiation into free space in agreement with the corresponding canonical Huygens current sheet pair results.

In contrast to the ideal cases in which the dipoles were matched to the lumped port by whatever input impedance they exhibited, i.e., by specifying their values, realistic HDAs matched to 50-Ω sources were developed. Several custom-designed HDAs were reported. Two were matched to a 50-Ω lumped port and two were matched to a 50-Ω coax feed. Each pair represented radiators in free space and on the high permittivity dielectric block for comparison purposes. It was firmly established that actual custom-designed HDAs placed on the interface would achieve the desired radiation physics, i.e., they could be designed to radiate efficiently in the broadside direction, primarily into the free space region away from the block with very small back radiation into it.

Furthermore, while the HDAs considered herein were transmitting systems, applications of an HDA system as a receiving OCA or wearable/on-body system were noted. Wireless power transfer (WPT) and energy harvesting (WEH) enable battery-less operation of SoCs and IoT sensors, a very recent and relevant thrust for many commercial applications. If the receiving patterns of an OCA or on-body device were primarily pointed towards the free space side of the high permittivity dielectric region on which they reside, they would significantly enhance the ability of on-chip and on-body WPT and WEH systems to capture a maximum amount of any incident power. Circularly polarized (CP) properties would further enhance their performance since they facilitate mitigation of any polarization mismatch issues. CP HDAs [17] and HDA-based rectennas [29] related to the custom-designed ones reported herein have been developed recently. The demonstration that NFRP HDAs can overcome a common OCA bottleneck coupled with their proven versatility of being tailorable to a variety of application environments such as on human bodies and their demonstrated high efficiencies suggest they have the potential to meet a variety of prerequisites of 5G wireless SoC-based and other IoT devices.

APPENDIX A
ADDITIONAL DETAILS OF THE CANONICAL PLANE WAVE ANALYSES

The electromagnetic plane wave fields radiated by infinite current sheets on the interface between two semi-infinite regions are obtained analytically. Electric and magnetic sources and their combinations are considered. With a balance of those sources prescribed by these analytical results, it is proved that the radiated fields can be made to reside completely in only one of the regions.

A. CANONICAL ELECTRIC AND MAGNETIC PROBLEMS IN A HOMOGENOUS REGION

The time-harmonic 3D Maxwell equations for the electromagnetic fields $\vec{E}, \vec{H}$ are:

$$\begin{aligned} \nabla \times \vec{E}_\omega &= -j\omega\,\mu\,\vec{H}_\omega - \vec{K}_\omega \\ \nabla \times \vec{H}_\omega &= j\omega\,\varepsilon\,\vec{E}_\omega + \vec{J}_\omega \end{aligned} \tag{13}$$

where the electric and magnetic currents sources are, respectively, $\vec{J}$ and $\vec{K}$, and the frequency and angular frequency of the sources are, respectively, f and $\omega = 2\pi f$. The canonical configurations considered take the sources to be infinite current sheets in the $z = 0$ plane and, hence, the resulting electromagnetic plane wave propagation to be along the z-axis. The medium is assumed to be a homogeneous, isotropic, linear, time-invariant region.

First, an electric current sheet is considered to be the source of the fields and is assumed to be x-directed. The time harmonic 1D Maxwell's equations for the resulting x-oriented (y-oriented) electric (magnetic) plane wave field are

$$\begin{aligned} \partial_z E_{\omega x} &= -j\omega\,\mu\,H_{\omega y} \\ \partial_z H_{\omega y} &= -j\omega\,\varepsilon\,E_{\omega x} - J_{\omega x} \end{aligned} \tag{14}$$

With $k^2 = \omega^2\,\varepsilon\,\mu$ this first-order system leads to the second-order Helmholtz equation

$$\partial_z^2 E_{\omega x} + k^2 E_{\omega x} = j\omega\,\mu\,J_{\omega x} \tag{15}$$

Second, a magnetic current sheet is considered to be the source of the fields and is assumed to be y-directed. The time harmonic 1D Maxwell's equations for the resulting y-oriented (x-oriented) magnetic (electric) plane wave field are

$$\begin{aligned} \partial_z E_{\omega x} &= -j\omega\,\mu\,H_{\omega y} - K_{\omega y} \\ \partial_z H_{\omega y} &= -j\omega\,\varepsilon\,E_{\omega x} \end{aligned} \tag{16}$$

Similarly, this system leads to the second-order Helmholtz equation

$$\partial_z^2 H_{\omega y} + k^2 H_{\omega y} = j\omega\,\varepsilon\,K_{\omega y} \tag{17}$$

The corresponding 1D Green's function for both of these Helmholtz equations is

$$G(z, z') = \frac{e^{-jk|z-z'|}}{2jk} \tag{18}$$

where

$$\partial_z^2 G + k^2 G = -\delta(z - z') \tag{19}$$

Consequently, the 1D solutions for both the electric and magnetic cases are the convolution of this Green's function with their forcing terms:

$$\begin{aligned} E_{\omega x,e} &= -j\omega\,\mu\,G * J_{\omega x} \\ H_{\omega y,m} &= -j\omega\,\varepsilon\,G * K_{\omega y} \end{aligned} \tag{20}$$

where $*$ represents the convolution operation.

B. ELECTRIC CURRENT SHEET ON THE INTERFACE BETWEEN TWO SEMI-INFINITE MEDIA

The electromagnetic field radiated by a time harmonic infinite electric current sheet sandwiched between two semi-infinite media follows naturally from the corresponding homogeneous region solutions. Region 2, $z > 0$, represents the semi-infinite region characterized by the parameters ε_2 and μ_2. Region 1, $z < 0$, represents the semi-infinite region characterized by the parameters ε_1 and μ_1. The boundary between the two semi-infinite half spaces is assumed to be the $z = 0$ plane. Thus, the electric current sheet lies on this interface. This configuration is shown in Fig. 1. The surface current sheet, as given by Eq. (1), and repeated here for convenience is defined simply as

$$\vec{J}_{\omega s} = J_0\,\delta(z)\,\hat{x} \tag{21}$$

The convolution-based Green's function expressions (20) for the plane wave fields in each source-free homogeneous Regions 1 and 2 yield, respectively:

$$\begin{aligned} \vec{E}_{\omega,e2} &= -j\omega\,\mu_2 A\,\frac{e^{-jk_2 z}}{2jk_2}\,\hat{x} = -\frac{A}{2}\,\eta_2\,e^{-jk_2 z}\,\hat{x} \\ \vec{H}_{\omega,e2} &= \frac{1}{-j\omega\,\mu_2}\,\partial_z\,E_{\omega x,e2}\,\hat{y} = -\frac{A}{2}\,e^{-jk_2 z}\,\hat{y} \end{aligned} \tag{22}$$

$$\begin{aligned} \vec{E}_{\omega,e1} &= -j\omega\,\mu_1 B\,\frac{e^{+jk_1 z}}{2jk_1}\,\hat{x} = -\frac{B}{2}\,\eta_1\,e^{+jk_1 z}\,\hat{x} \\ \vec{H}_{\omega,e1} &= \frac{1}{-j\omega\,\mu_1}\,\partial_z\,E_{\omega x,e1}\,\hat{y} = +\frac{B}{2}\,e^{+jk_1 z}\,\hat{y} \end{aligned} \tag{23}$$

where A and B are arbitrary constant amplitudes and the wave impedance and wave number of the regions are $\eta_\ell = \sqrt{\mu_\ell/\varepsilon_\ell}$ and $k_\ell = \omega^2\,\sqrt{\varepsilon_\ell\,\mu_\ell}$ for $\ell = 1, 2$. The subscript "e" labels these electric current results.

One then determines A and B by enforcing the electromagnetic boundary conditions for this configuration, i.e., the interface conditions: $-\hat{n} \times (\vec{E}_{\omega,e2} - \vec{E}_{\omega,e1})|_{z=0} = 0$ and $\hat{n} \times (\vec{H}_{\omega,e2} - \vec{H}_{\omega,e1})|_{z=0} = \vec{J}_{\omega s}$, where $\hat{n}$ is the unit normal to the interface pointing from Region 1 into Region 2. These interface expressions yield the explicit conditions:

$$\begin{aligned} E_{\omega x,e2}(z=0) &= E_{\omega x,e1}(z=0) \\ -H_{\omega y,e2}(z=0) &+ H_{\omega y,e1}(z=0) = J_0 \end{aligned} \tag{24}$$

Applying these interface conditions, one obtains $\eta_2\,A = \eta_1\,B$ and $A + B = 2\,J_0$. Consequently, the amplitudes of the fields are determined to be

$$\begin{aligned} A &= \frac{2\,J_0}{1 + \eta_2/\eta_1} = \frac{2\,\eta_1}{\eta_1 + \eta_2}\,J_0 \\ B &= \frac{2\,\eta_2}{\eta_1 + \eta_2}\,J_0 \end{aligned} \tag{25}$$

Therefore, the electromagnetic fields in both regions are:

$$\begin{aligned} \vec{E}_{\omega,e2} &= -\frac{\eta_1\,\eta_2}{\eta_1 + \eta_2}\,J_0\,e^{-jk_2 z}\,\hat{x} \\ \vec{H}_{\omega,e2} &= -\frac{\eta_1}{\eta_1 + \eta_2}\,J_0\,e^{-jk_2 z}\,\hat{y} \end{aligned} \tag{26}$$

$$\vec{E}_{\omega,e1} = -\frac{\eta_1\,\eta_2}{\eta_1+\eta_2}\,J_0\,e^{+jk_1z}\,\hat{x}$$
$$\vec{H}_{\omega,e1} = +\frac{\eta_2}{\eta_1+\eta_2}\,J_0\,e^{+jk_1z}\,\hat{y} \qquad (27)$$

One clearly sees that the electric fields are continuous across the electric current sheet at $z = 0$, and the corresponding discontinuity in the magnetic fields recovers the source term. The power density expressions given in Section II.A follow immediately.

C. MAGNETIC CURRENT SHEET ON THE INTERFACE BETWEEN TWO SEMI-INFINITE MEDIA

The electromagnetic fields radiated by a time harmonic infinite magnetic current sheet sandwiched between two semi-infinite media follow straightforwardly as in the electric case (or simply by duality). Let the magnetic current sheet be defined as

$$\vec{K}_s = K_0\,\delta(z)\,\hat{y} \qquad (28)$$

The interface conditions: $\hat{n}\times(\vec{H}_{\omega,m2}-\vec{H}_{\omega,m1})|_{z=0} = 0$ and $-\hat{n}\times(\vec{E}_{\omega,m2}-\vec{E}_{\omega,m1})|_{z=0} = \vec{K}_{\omega s}$ yield the explicit conditions:

$$H_{\omega y,e2}(z=0) = H_{\omega y,e1}(z=0)$$
$$-E_{\omega x,e2}(z=0) + E_{\omega x,e1}(z=0) = K_0 \qquad (29)$$

Applying these interface conditions and solving for the unknown field amplitudes in each region, one obtains

$$\vec{H}_{\omega,m2} = -\frac{1}{\eta_1+\eta_2}\,K_0\,e^{-j\,k_2\,z}\,\hat{y}$$
$$\vec{E}_{\omega,m2} = -\frac{\eta_2}{\eta_1+\eta_2}\,K_0\,e^{-j\,k_2\,z}\,\hat{x} \qquad (30)$$
$$\vec{H}_{\omega,m1} = -\frac{1}{\eta_1+\eta_2}\,K_0\,e^{+j\,k_1\,z}\,\hat{y}$$
$$\vec{E}_{\omega,m1} = +\frac{\eta_1}{\eta_1+\eta_2}\,K_0\,e^{+j\,k_1\,z}\,\hat{x} \qquad (31)$$

where the ''m'' labels these magnetic current results.

Consequently, the associated time averaged power density in each region is:

$$\left\langle\vec{S}_{\omega,m2}\right\rangle = +\frac{1}{2}\,\frac{\eta_2}{|\eta_1+\eta_2|^2}\,|K_0|^2\,\hat{z}$$
$$\left\langle\vec{S}_{\omega,m1}\right\rangle = -\frac{1}{2}\,\frac{\eta_1}{|\eta_1+\eta_2|^2}\,|K_0|^2\,\hat{z} \qquad (32)$$

These expressions give the ratio of the power radiated into each region as:

$$\frac{\left\langle\vec{S}_{\omega,m2}\right\rangle\cdot\hat{z}}{-\left\langle\vec{S}_{\omega,m1}\right\rangle\cdot\hat{z}} = \frac{\eta_2}{\eta_1} \qquad (33)$$

Now, as was done for the electric current case in Section II, consider both regions to be non-magnetic. The power flow ratio (33) becomes

$$\frac{\left\langle\vec{S}_{\omega,m2}\right\rangle\cdot\hat{z}}{-\left\langle\vec{S}_{\omega,m1}\right\rangle\cdot\hat{z}} = (\varepsilon_1)^{1/2} = n_1 \qquad (34)$$

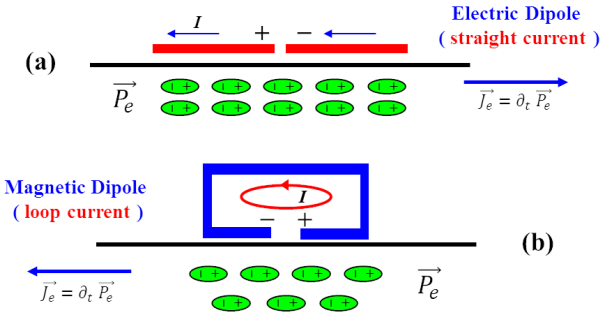

FIGURE 19. Polarization currents established when an electric dipole and a magnetic dipole lie on a high dielectric region.

Thus, even if the dielectric has a large permittivity, a larger portion of the radiated power will reside in Region 2, free space. Again using silicon as an example, 3.42 times more power is radiated by the magnetic source into Region 2 than into Region 1. On the other hand, if Region 1 was magnetic with a high permeability, e.g., $\varepsilon_1 = \varepsilon_0$ and $\mu_1 > \mu_0$, then more power radiated from the magnetic current would be pulled into it.

The outcome in the dielectric case makes physical sense since the magnetic source interacts with the dielectric Region 1 much less than an electric source does. To better explain this effect and to connect it to the results in Section III and IV, consider the configuration illustrated in Fig. 19. The linear current on the electric dipole radiator is parallel to the interface. The resulting electric field induces strong polarization currents in the dielectric near the interface and further away from it. These lead to the large fields emitted into the dielectric, as well as a partial cancellation of the fields emitted by the dipole into the air region. In contrast, the electric field generated by the loop current of the magnetic dipole induces weaker polarization currents in the dielectric that partially reinforces (cancels) the field in the air (dielectric) region. Consequently, a magnetic radiator as an OCA or on-body antenna has an unique advantage over the traditional choice of an electric one. It naturally emits more power into free space than into the dielectric. Nevertheless, the Huygens source represents a fundamentally better resolution to the problem as demonstrated next and summarized in Section II.

D. ELECTRIC AND MAGNETIC CURRENT SHEETS ON THE INTERFACE BETWEEN TWO SEMI-INFINITE MEDIA

Finally, consider the electromagnetic field radiated when orthogonal time harmonic infinite electric and magnetic current sheets, Eqs. (21) and (28), respectively, are sandwiched between two semi-infinite media. This configuration is shown in Fig. 2. The total fields in both regions follow immediately by the superposition of the two independent electric and magnetic current sheet solutions. They are

$$\vec{E}_{\omega,\text{total }2} = \left[-\left(\frac{\eta_1\,\eta_2}{\eta_1+\eta_2}\right)J_0 - \left(\frac{\eta_2}{\eta_1+\eta_2}\right)K_0\right]e^{-j\,k_2\,z}\,\hat{x}$$
$$= -\left(\frac{\eta_2}{\eta_1+\eta_2}\right)\left[\,\eta_1\,J_0 + K_0\,\right]e^{-j\,k_2\,z}\,\hat{x}$$

$$\vec{H}_{\omega,\text{total 2}} = \left[-\left(\frac{\eta_1}{\eta_1+\eta_2}\right) J_0 - \left(\frac{1}{\eta_1+\eta_2}\right) K_0 \right] e^{-jk_2 z}\,\hat{y}$$
$$= -\left(\frac{1}{\eta_1+\eta_2}\right) [\,\eta_1 J_0 + K_0\,]\, e^{-jk_2 z}\,\hat{y} \quad (35)$$
$$\vec{E}_{\omega,\text{total 1}} = \left[-\left(\frac{\eta_1\,\eta_2}{\eta_1+\eta_2}\right) J_0 + \left(\frac{\eta_1}{\eta_1+\eta_2}\right) K_0 \right] e^{+jk_1 z}\,\hat{x}$$
$$= -\left(\frac{\eta_1}{\eta_1+\eta_2}\right) [\,\eta_2 J_0 - K_0\,]\, e^{+jk_1 z}\,\hat{x}$$
$$\vec{H}_{\omega,\text{total 1}} = \left[+\left(\frac{\eta_2}{\eta_1+\eta_2}\right) J_0 - \left(\frac{1}{\eta_1+\eta_2}\right) K_0 \right] e^{+jk_1 z}\,\hat{y}$$
$$= \left(\frac{1}{\eta_1+\eta_2}\right) [\,\eta_2 J_0 - K_0\,]\, e^{+jk_1 z}\,\hat{y} \quad (36)$$

Consequently, if the electric and magnetic currents are balanced, i.e., if

$$K_0 = \eta_2 J_0 \quad (37)$$

then the total fields in each region represent a "Huygens" plane wave, i.e., the combined fields from the electric and magnetic current sources are non-zero only in Region 2:

$$\vec{E}_{\omega 2,\text{total}} = -\eta_2 J_0\, e^{-jk_2 z}\,\hat{x}$$
$$\vec{H}_{\omega 2,\text{total}} = -J_0\, e^{-jk_2 z}\,\hat{y}$$
$$\vec{E}_{\omega 1,\text{total}} = 0$$
$$\vec{H}_{\omega 1,\text{total}} = 0 \quad (38)$$

and, hence, the time averaged total radiated power density in both regions is:

$$\left\langle \vec{S}_{\omega 2,\text{total}} \right\rangle = +\frac{1}{2}\,\eta_2\,|J_0|^2\,\hat{z}$$
$$\left\langle \vec{S}_{\omega 1,\text{total}} \right\rangle = 0 \quad (39)$$

Therefore, with the tailored balance (37) of the electric and magnetic current sources with respect to the impedance of Region 2, one recovers the plane wave fields that would exist if both regions were free space and the equivalent currents derived from a plane wave propagating only in the +z-direction were specified on the plane $z = 0$.

Carefully examining the expression, for example, of the combined electric field in Region 2, one finds that the electric current contribution is weighted by the impedance of Region 1 and, hence, is decreased if Region 1 were a dielectric (i.e., if $\varepsilon_1 > \varepsilon_2 = \varepsilon_0$, then $\eta_1 < \eta_2 = \eta_0$). The corresponding electric current contribution in Region 1 is then greater since it is weighted by the free-space impedance. Without the magnetic current, these effective currents explain why the electric fields in the dielectric case are larger in Region 1 than in Region 2. The balanced condition (37) is then seen to "rebalance" the magnetic current contribution so that it matches the effective electric currents in Region 1. This balance was able to facilitate the complete cancellation of the fields in the back direction, yielding a total zero field in Region 1, as it was for the ideal radiators considered in the Huygens dipole array considered in Section III.B.

In the same manner, the other balanced condition choice:

$$K_0 = -\eta_1 J_0 \quad (40)$$

yields zero total fields in Region 2 and an emitted Huygens plane wave propagating solely in Region1:

$$\vec{E}_{\omega 2,\text{total}} = 0$$
$$\vec{H}_{\omega 2,\text{total}} = 0 \quad (41)$$
$$\vec{E}_{\omega 1,\text{total}} = -\eta_1 J_0\, e^{+jk_1 z}\,\hat{x}$$
$$\vec{H}_{\omega 1,\text{total}} = J_0\, e^{+jk_1 z}\,\hat{y} \quad (42)$$

with the corresponding power densities in each region:

$$\left\langle \vec{S}_{\omega 2,\text{total}} \right\rangle = 0$$
$$\left\langle \vec{S}_{\omega 1,\text{total}} \right\rangle = -\frac{1}{2}\,\eta_1\,|J_0|^2\,\hat{z} \quad (43)$$

Thus the tailored balance (40) yields a power flow radiating into the opposite direction from the previous case. This outcome occurs because of the opposite orientation of the magnetic current and a re-balance of its magnitude relative to the electric current, as was necessary with the Huygens dipole array in Section III.C.

Even though they are only 1D plane wave results, these analytical derivations provided the incentive to demonstrate that a custom-designed Huygens dipole antenna system could be developed that would radiate more effectively either away from or into the high permittivity substrate on which it is positioned.

APPENDIX B
SIMULATED IDEAL MAGNETIC DIPOLE ELEMENTS

The electrically small magnetic dipole (loop) configuration corresponding to the electric dipole case considered in Section II is shown in Fig. 20. Recall that it is driven by a voltage source located in a gap at the center of its side on the interface. The simulated 2D directivity patterns of this small loop antenna in free space at the source frequency $f_0 = 300$ MHz are shown in Fig. 21a. It has a maximum directivity in free space $m1 = 1.49$ dB. The directivity pattern in the $\phi = 0°$ plane orthogonal to the loop has the well-known doughnut shape and the pattern in the $\phi = 90°$ plane, which contains the loop, is omnidirectional [20]. Since $m2 = 1.49$ dB, the $FTBR = 0$ dB (1.0).

In comparison, the simulated 2D directivity patterns of this loop on the interface of the block at f_0 are given in Fig. 21b, repeated here for convenience from Fig. 8. The patterns are pointed primarily away from the block into free space along the normal to the interface. The maximum directivity $m1 = 6.78$ dB is along the +z-axis. The directivity in the antipodal direction is $m2 = -0.44$ dB. Hence, the $FTBR = 7.22$ dB.

These results are essentially opposite to the electric case outcomes as expected from the 1D analytical considerations discussed in Appendix A. Notice that similar to the electric dipole case, the omnidirectional behavior is significantly altered in the presence of the block and the polarization

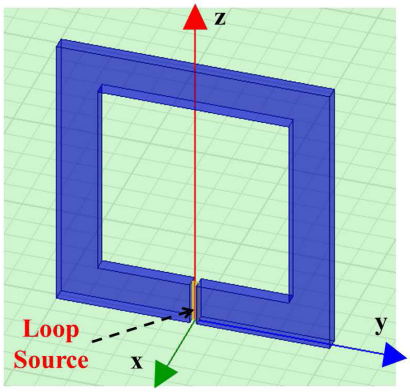

FIGURE 20. 3D problem: Electrically small magnetic dipole antenna centered on the high permittivity block.

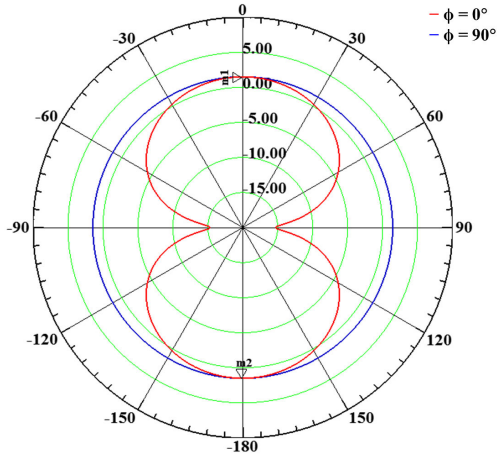

(a) Free space

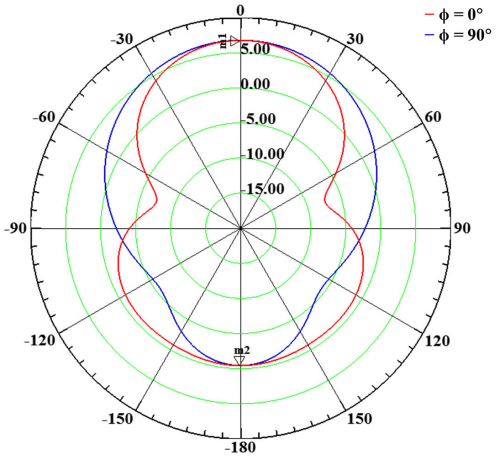

(b) Dielectric block

FIGURE 21. Simulated 2D directivity patterns at f_0 of the electrically small magnetic dipole antenna centered on the high permittivity block with its source on its bottom segment.

currents induced in it. While the maximum directivity in both planes is again the same, the difference between the two principal plane patterns is not as great as it was in the

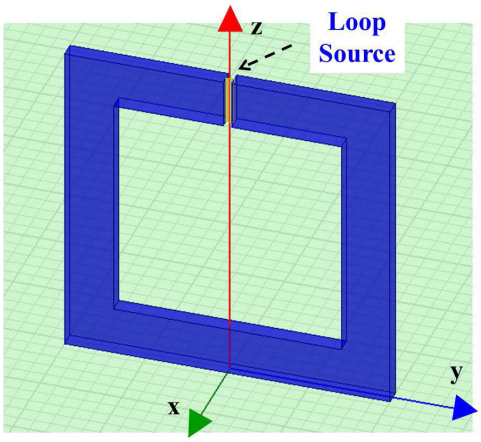

(a) Source on the top side of the loop

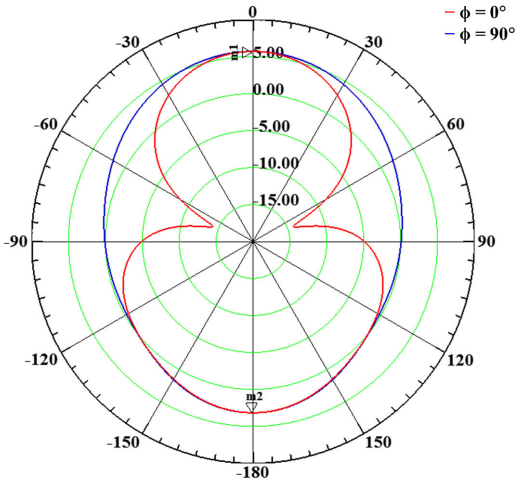

(b) 2D directivity patterns at f_0

FIGURE 22. Simulated electrically small magnetic dipole antenna centered on the high permittivity block with its source on its top segment.

electric case. This coincides with the fact that the dielectric has much less impact on the radiation physics associated with a magnetic source.

An unexpected behavior was noticed during the configuration studies. Clearly, the gap source could be centered on any side of the loop. The top and the bottom locations are the most symmetrical for the desired behaviors, i.e., away from or into the block. The loop centered on the interface of the block with its source centered on its top side is depicted in Fig. 22a. The corresponding simulated 2D directivity patterns at f_0 are given in Fig. 22b and are noticeably different from those in Fig. 21b. With $m2 = 3.16$ dB, much more of the radiated power is directed into the block even though the maximum directivity $m1 = 5.71$ dB is still along the +z-axis. As a consequence, the patterns have narrower beamwidths. Moreover, the *FTBR* in now only 2.55 dB.

Realizing that the current density is strongest along the side of the loop opposite its voltage source, it became clear why the source on the top side of the loop pushed more field into

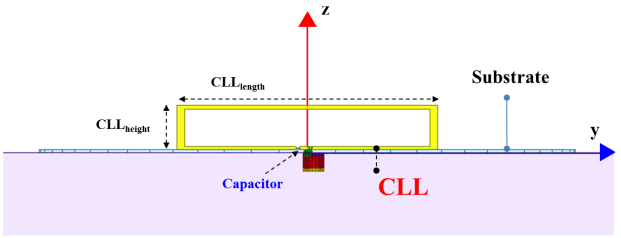

FIGURE 23. Side view of the coax-fed CLL-only NFRP antenna on the high permittivity block.

the block. With the strong current density being directly on the interface in this configuration, the bottom segment acts more like an electric dipole and more power is directed into the block than with the source on the bottom segment. With the source on the bottom segment, the opposite, top segment is the one with the strongest current on it. Since it is displaced far from the interface, it radiates more effectively into the free space region.

These observations dictated the location of the source of the loop to be on the bottom segment for the ideal Huygens source case that radiates primarily into the air region. They also provided the reason why the source is on the top segment for the ideal Huygens dipole array designed to radiate into the high permittivity block.

APPENDIX C
COAX-FED CLL-ONLY NFRP ANTENNA ON THE BLOCK

To illustrate the impact of the combined electrical and magnetic NFRP elements on the overall performance, the corresponding coax-fed CLL-only NFRP antenna was also simulated. It represents a realistic version of the ideal loop case considered in Appendix B. The configuration was obtained from the coax-fed HDA by simply deleting the entire EAD element, i.e., the associated substrate, the EAD element and its inductors. A side view of the resulting antenna on the block is shown in Fig. 23.

The only parameters changed to achieve matching at a frequency near to f_0 were: $C = 4.0$ pF and $\text{Dipole}_{\text{length}} = 62.0$ mm. The simulated performance characteristics are presented in Fig. 24. The $|S_{11}|$ values in Fig. 24(a) indicate that its minimum reflection coefficient, -42.23 dB, with respect to the 50-Ω source occurs at $f_{res} = 299.820$ MHz. With this resonance frequency, one finds $ka = 0.45$. The 2D directivity patterns in the principal planes are given in Fig. 24(b). The directivity values $m1 = 6.74$ dB and $m2 = -1.67$ dB along the z-axis give $FTBR = 8.41$ dB. The radiation efficiency is 88.45%.

Comparing Fig. 24(b) to Fig. 18(b) it is clear that the HDA significantly reduces the power radiated into the dielectric block. Nonetheless, as noted in Section III, the performance of the magnetic radiator itself is significantly better than that of the electric radiator alone. The recognition of this property suggests that magnetic radiators could also be useful, even if they do not perform as well as the HDAs do. They would particularly be useful themselves in situations

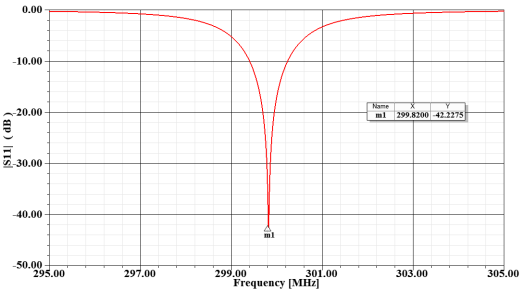

(a) $|S_{11}|$ values versus frequency

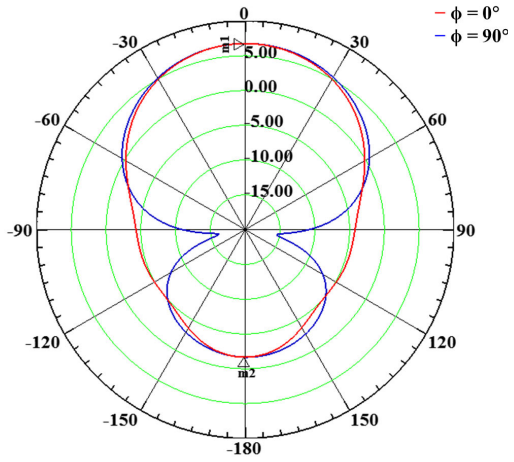

(b) Simulated 2D directivity patterns at f_{res}

FIGURE 24. Electrically small coax-fed CLL-only NFRP antenna centered on the high permittivity block.

where, for example, the OCA is placed above a ground plane. A horizontal magnetic dipole naturally facilitates low profile designs in such configurations.

ACKNOWLEDGMENT

The author would like to thank Dr. H. Sun, currently with the Nanyang Technological University in Singapore, very much for her time and efforts in carefully proofreading the original version of this article.

REFERENCES

[1] A. Babakhani, G. Xiang, A. Komijani, A. Natarajan, and A. Hajimiri, "A 77-GHz phased-array transceiver with on-chip antennas in silicon: Receiver and antennas," *IEEE J. Solid-State Circuits*, vol. 41, no. 12, pp. 2795–2806, Dec. 2006.

[2] A. Babakhani, D. B. Rutledge, and A. Hajimiri, "Near-field direct antenna modulation," *IEEE Microw. Mag.*, vol. 10, no. 1, pp. 36–46, Feb. 2009.

[3] S. Radiom, K. Mohammadpour-Aghdam, G. A. E. Vandenbosch, and G. Gielen, "A monolithically integrated on-chip antenna in 0.18 μm standard CMOS technology for far-field short-range wireless powering," *IEEE Antennas Wireless Propag. Lett.*, vol. 9, pp. 631–633, 2010.

[4] H. M. Cheema and A. Shamim, "The last barrier: On-chip antennas," *IEEE Microw. Mag.*, vol. 14, no. 1, pp. 79–91, Jan./Feb. 2013.

[5] Y. Song, K. Kang, Y. Tian, Y. Wu, Z. Li, Y. Guo, Y. Ban, J. Liu, X. Tang, H. Liu, and J. Yang, "A hybrid integrated high-gain antenna with an on-chip radiator backed by off-chip ground for system-on-chip applications," *IEEE Trans. Compon., Packag., Manuf. Technol.*, vol. 7, no. 1, pp. 114–122, Jan. 2017.

[6] S. Mandal, S. K. Mandal, and A. K. Mal, "On-chip antennas using standard CMOS technology: A brief overview," in *Proc. Int. Conf. Innov. Electron., Signal Process. Commun. (IESC)*, Shillong, India, Apr. 2017, pp. 74–78.

[7] T. Zwick, F. Boes, B. Göttel, A. Bhutani, and M. Pauli, "Pea-sized mmW transceivers: QFN-based packaging concepts for millimeter-wave transceivers," *IEEE Microw. Mag.*, vol. 18, no. 6, pp. 79–89, Sep./Oct. 2017.
[8] F. Lin and B. L. Ooi, "Integrated millimeter-wave on-chip antenna design employing artificial magnetic conductor," in *Proc. IEEE Int. Symp. Radio-Freq. Integr. Technol. (RFIT)*, Singapore, Jan./Dec. 2009, pp. 174–177.
[9] X.-Y. Bao, Y.-X. Guo, and Y.-Z. Xiong, "60-GHz AMC-based circularly polarized on-chip antenna using standard 0.18-μm CMOS technology," *IEEE Trans. Antennas Propag.*, vol. 60, no. 5, pp. 2234–2241, May 2012.
[10] M. Nafe, A. Syed, and A. Shamim, "Gain enhancement of low profile on-chip dipole antenna via artificial magnetic conductor at 94 GHz," in *Proc. 9th Eur. Conf. Antennas Propag. (EuCAP)*, Lisbon, Portugal, Apr. 2015, pp. 1–3.
[11] H. Zhang and A. Shamim, "Gain and efficiency enhancement of a 77 GHz on-chip antenna through AMC and superstrate package," in *Proc. IEEE Int. Symp. Antennas Propag. USNC/URSI Nat. Radio Sci. Meeting*, Boston, MA, USA, Jul. 2018, pp. 363–364.
[12] P. S. Hall, Y. Hao, Yuriy I. Nechayev, A. Alomainy, C. C. Constantinou, C. Parini, M. R. Kamarudin, T. Z. Salim, D. T. M. Hee, R. Dubrovka, A. S. Owadally, W. Song, A. Serra, P. Nepa, M. Gallo, and M. Bozzetti, "Antennas and propagation for on-body communication systems," *IEEE Antennas Propag. Mag.*, vol. 49, no. 3, pp. 41–58, Jun. 2007.
[13] K. N. Paracha, S. K. A. Rahim, P. J. Soh, and M. Khalily, "Wearable antennas: A review of materials, structures, and innovative features for autonomous communication and sensing," *IEEE Access*, vol. 7, pp. 56694–56712, 2019.
[14] R. Pethig, "Dielectric properties of body tissues," *Clin. Phys. Physiol. Meas.*, vol. 8, pp. 5–12, Jan. 1987.
[15] R. W. Ziolkowski, "Low profile, broadside radiating, electrically small Huygens source antennas," *IEEE Access*, vol. 3, pp. 2644–2651, 2015.
[16] M.-C. Tang, H. Wang, and R. W. Ziolkowski, "Design and testing of simple, electrically small, low-profile, Huygens source antennas with broadside radiation performance," *IEEE Trans. Antennas Propag.*, vol. 64, no. 11, pp. 4607–4617, Nov. 2016.
[17] W. Lin and R. W. Ziolkowski, "Electrically small, low-profile, Huygens circularly polarized antenna," *IEEE Trans. Antennas Propag.*, vol. 66, no. 2, pp. 636–643, Feb. 2018.
[18] N. Engheta, C. H. Papas, and C. Elachi, "Radiation patterns of interfacial dipole antennas," *Radio Sci.*, vol. 17, no. 6, pp. 1557–1566, 1982.
[19] G. S. Smith, "Directive properties of antennas for transmission into a material half-space," *IEEE Trans. Antennas Propag.*, vol. 32, no. 3, pp. 232–246, Mar. 1984.
[20] C. A. Balanis, *Antenna Theory: Analysis and Design*. Hoboken, NJ, USA: Wiley, 2016.
[21] M.-C. Tang, T. Shi, and R. W. Ziolkowski, "A study of 28 GHz, planar, multilayered, electrically small, broadside radiating, Huygens source antennas," *IEEE Trans. Antennas Propag.*, vol. 65, no. 12, pp. 6345–6354, Dec. 2017.
[22] R. W. Ziolkowski, "Using Huygens multipole arrays to realize unidirectional needle-like radiation," *Phys. Rev. X*, vol. 7, no. 3, Jul. 2017, Art. no. 031017.
[23] W. Lin and R. W. Ziolkowski, "Wirelessly powered light and temperature sensors facilitated by electrically small omnidirectional and Huygens dipole antennas," *Sensors*, vol. 19, no. 9, p. 1998, Apr. 2019.
[24] W. Lin and R. W. Ziolkowski, "Electrically small Huygens antenna-based fully-integrated wireless power transfer and communication system," *IEEE Access*, vol. 7, pp. 39762–39769, 2019.
[25] M.-C. Tang, T. Shi, and R. W. Ziolkowski, "Electrically small, broadside radiating Huygens source antenna augmented with internal non-Foster elements to increase its bandwidth," *IEEE Antennas Wireless Propag. Lett.*, vol. 16, pp. 712–715, 2017.
[26] N. Zhu and R. W. Ziolkowski, "Broad-bandwidth, electrically small antenna augmented with an internal non-Foster element," *IEEE Antennas Wireless Propag. Lett.*, vol. 11, pp. 1116–1120, 2012.
[27] N. Zhu and R. W. Ziolkowski, "Broad bandwidth, electrically small, non-Foster element-augmented antenna designs, analyses, and measurements," *IEICE Trans. Commun.*, vol. 96, no. 10, pp. 2399–2409, Oct. 2013.
[28] M.-C. Tang, N. Zhu, and R. W. Ziolkowski, "Augmenting a modified Egyptian axe dipole antenna with non-Foster elements to enlarge its directivity bandwidth," *IEEE Antennas Wireless Propag. Lett.*, vol. 12, pp. 421–424, 2013.
[29] W. Lin, R. W. Ziolkowski, and J. Huang, "Electrically small, low-profile, highly efficient, Huygens dipole rectennas for wirelessly powering Internet-of-Things devices," *IEEE Trans. Antennas Propag.*, vol. 67, no. 6, pp. 3670–3679, Jun. 2019.

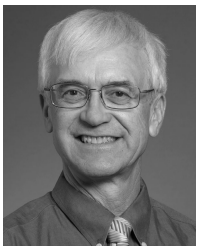

RICHARD W. ZIOLKOWSKI (M'87–SM'91–F'94) received the B.Sc. degree *(magna cum laude)* (Hons.) in physics from Brown University, Providence, RI, USA, in 1974, the M.S. and Ph.D. degrees in physics from the University of Illinois at Urbana–Champaign, Urbana, IL, USA, in 1975 and 1980, respectively, and the Honorary Doctorate degree from the Technical University of Denmark, Kongens Lyngby, Denmark, in 2012.

He was the Computational Electronics and Electromagnetics Thrust Area Leader with the Lawrence Livermore National Laboratory, Engineering Research Division, Tucson, AZ, USA, in 1990. He was a Professor Emeritus with The University of Arizona, in 2018, where he was a Litton Industries J. M. Leonis Distinguished Professor with the Department of Electrical and Computer Engineering, College of Engineering, and also a Professor with the College of Optical Sciences. He is currently a Distinguished Professor with the Global Big Data Technologies Centre, Faculty of Engineering and Information Technologies (FEIT), University of Technology Sydney, Ultimo, NSW, Australia. His current research interests include the application of new mathematical and numerical methods to linear and nonlinear problems dealing with the interaction of electromagnetic and acoustic waves with complex linear and nonlinear media, and meta materials, meta material-inspired structures, nano-structures, and other classical and quantum applications-specific configurations.

Prof. Ziolkowski is a Fellow of the Optical Society of America (OSA, 2006) and the American Physical Society (APS, 2016). He was the recipient of the 2019 IEEE Electromagnetics Award (IEEE Technical Field Award). He served as the President for the IEEE Antennas and Propagation Society, in 2005. He is also actively involved with the URSI, OSA, and SPIE professional societies. He was the Australian DSTO Fulbright Distinguished Chair in Advanced Science and Technology, from 2014 to 2015. He was a 2014 Thomas-Reuters Highly Cited Researcher.